Cavendish–HEP–96/3
DFTT 19/96
March 1996

The process $e^+e^- \rightarrow b\bar{b}W^+W^-$ at the Next Linear Collider in the Minimal Supersymmetric Standard Model

Stefano Moretti[1]

Cavendish Laboratory, University of Cambridge,
Madingley Road, Cambridge, CB3 0HE, United Kingdom.

Dipartimento di Fisica Teorica, Università di Torino, Italy
and INFN, Sezione di Torino
Via Pietro Giuria 1, 10125 Torino, Italy.

Abstract

The complete matrix element for $e^+e^- \rightarrow b\bar{b}W^+W^-$ is computed at tree-level within the Minimal Supersymmetric Standard Model. Rates of interest to phenomenological analyses at the Next Linear Collider are given. In particular, we study:

- $t\bar{t}$ production and decay $t\bar{t} \rightarrow (bW^+)(\bar{b}W^-)$;
- ZH production followed by $Z \rightarrow b\bar{b}$ and $H \rightarrow W^+W^-$;
- AH production followed by $A \rightarrow b\bar{b}$ and $H \rightarrow W^+W^-$;
- hW^+W^- production followed by $h \rightarrow b\bar{b}$.

Top and Higgs finite width effects are included, as well as all those of the irreducible backgrounds.

[1]E-mails: moretti@hep.phy.cam.ac.uk,moretti@to.infn.it.

1. Introduction

By the time that the Next Linear Collider (NLC) [1] will be operating, both the exact value of the top quark mass and the structure of the Higgs sector of the electroweak (EW) interactions will be already known, thanks to the combined action of the Tevatron [2], of LEP II [3] and of the LHC [4, 5]. It is however clear that detailed studies of both top quark and Higgs boson properties will have to wait the advent of an e^+e^- linear machine.

In two previous papers [6, 7] detailed studies of the process $e^+e^- \rightarrow b\bar{b}W^+W^-$ at centre-of-mass (CM) energies typical of the NLC were presented. Those analyses were concerning the Standard Model ($\mathcal{SM}$). In that framework, the importance of the process $e^+e^- \rightarrow b\bar{b}W^+W^-$ is evident if one considers that it represents a signature to top production in $t\bar{t}$ pairs as well as to that of the $\mathcal{SM}$ Higgs boson ϕ in the $Z\phi$ channel. In fact, on the one hand, top pairs produced via the process $e^+e^- \rightarrow t\bar{t}$ decay through $t\bar{t} \rightarrow (bW^+)(\bar{b}W^-)$ whereas, on the other hand, the channel $Z\phi \rightarrow (b\bar{b})(W^+W^-)$ might well be one of best ways to detect a heavy Higgs, thanks to the expected performances of the vertex detectors in triggering the Z boson [8][2]. From those studies, the importance of top finite width effects and of those due to the non-resonant background in $b\bar{b}W^+W^-$ events clearly came out, together with positive prospects of Higgs detection.

It is the purpose of this report to extend those analyses to the case of the Minimal Supersymmetric Standard Model ($\mathcal{MSSM}$). In this context, the reaction $e^+e^- \rightarrow b\bar{b}W^+W^-$ is important in at least four respects. First and second, like in the $\mathcal{SM}$, it allows studies of top pair production and decay $t\bar{t} \rightarrow (bW^+)(\bar{b}W^-)$ as well as of the Higgs channel $ZH \rightarrow (b\bar{b})(W^+W^-)$. Third and fourth, it also allows one to analyse Higgs production in the channels $e^+e^- \rightarrow AH \rightarrow (b\bar{b})(W^+W^-)$ and $e^+e^- \rightarrow hW^+W^- \rightarrow (b\bar{b})W^+W^-$.

In particular, we notice that the $\mathcal{SM}$-like channel $t \rightarrow bW^\pm$ is the dominant top decay mechanism over a large part of the $\mathcal{MSSM}$ parameter space, especially if the mass of the charged Higgs boson $H^\pm$ is comparable to m_t, such that the decay channel $t \rightarrow bH^\pm$ is strongly suppressed by the available phase space[3] [10]. Conversely, when this is not the case, finite width effects should be more important in the $\mathcal{MSSM}$ [11, 12], as for $M_{H^\pm} < m_t - m_b$ (i.e., small values of M_A) one gets $\Gamma_t^{\mathcal{MSSM}} > \Gamma_t^{\mathcal{SM}}$. Furthermore, the process $e^+e^- \rightarrow ZH$ is nothing else than counterpart of the $\mathcal{SM}$ Higgs bremsstrahlung mechanism, where the heaviest of the neutral scalar Higgses of the $\mathcal{MSSM}$, H, plays the rôle of ϕ [13]. Finally, the decays $h, A \rightarrow b\bar{b}$ (of the light scalar and of the pseudoscalar Higgs bosons, respectively) and $H \rightarrow W^+W^-$ can be the dominant ones of these particles over a sizable portion of the plane $(M_A, \tan\beta)$, with the rates of $e^+e^- \rightarrow AH$ being comparable to those of $e^+e^- \rightarrow ZH$ [14] and the cross sections for $e^+e^- \rightarrow hW^+W^-$ being possibly of a few picobarns for $M_h \lesssim 100$ GeV (the increased $hb\bar{b}$ coupling compensating the reduced hW^+W^- one, with respect to

[2]The mode $Z \rightarrow b\bar{b}$ has a branching ratio (BR) about five times larger than the BRs into $\mu^+\mu^-$ or e^+e^- and it is equally free from backgrounds coming from W decays.

[3]Throughout this paper we assume that the mass scale of the Supersymmetric partners of the ordinary elementary particles is well beyond the energy reach of the NLC, such that they cannot be produced at this machine. In particular, we neglect here considering the Supersymmetric decay $t \rightarrow \tilde{t}\tilde{\chi}_1^0$, where $\tilde{t}$ represents the stop and $\tilde{\chi}_1^0$ refers to the lightest neutralino, as well as other possible $\mathcal{MSSM}$ modes. For a recent review of these latter, see Ref. [9].

the corresponding $\mathcal{SM}$ values).

We further remind the reader that the four processes $e^+e^- \to t\bar{t}$, $e^+e^- \to ZH$, $e^+e^- \to AH$ and $e^+e^- \to hW^+W^-$ cannot be unambiguously separated, and studied independently one from the others. Therefore any of them constitutes an irreducible background to the other three in the $b\bar{b}W^+W^-$ channel, and such interplay must be carefully taken into account when studying full $e^+e^- \to b\bar{b}W^+W^-$ events. As we are here computing the complete Matrix Element (ME) of such a process, also non-resonant background effects will be present. In this respect, diagrams involving the lightest $\mathcal{MSSM}$ neutral Higgs h, in which this is produced either far below threshold (in the splitting $h^* \to W^+W^-$) or in association with a off-shell Z (via $Z^* \to W^+W^-$), must be regarded as background.

The plan of the paper is as follows. In the next Section we describe the calculation we have performed; in Section 3 we present our results, whereas the conclusions are given in Section 4.

2. Calculation

In the $\mathcal{MSSM}$ the process

$$e^+e^- \to b\bar{b}W^+W^- \tag{1}$$

proceeds at tree-level through 75 Feynman diagrams, which can be conveniently grouped in 28 different topologies. Of these latter, 19 correspond to actual $\mathcal{SM}$ graphs, 8 to Higgs processes with $\mathcal{SM}$-like structure (in which a superposition of the h and H bosons replaces the ϕ scalar) and 2 to typical $\mathcal{MSSM}$ graphs involving a vertex with two (different) Higgs scalars and one vector boson. The first 27 topologies can be found in Refs. [6, 7], whereas the last one is depicted in Fig. 1.

To compute the amplitude squared of process (1) we have used two different spinor formalisms, described in Refs. [15, 16]. The results produced by the two corresponding `FORTRAN` codes agree within 10 significative digits in `REAL*8` precision. Moreover, the amplitude produced with the method of Ref. [16] has been tested for gauge invariance, as it has been implemented in three different gauges (Unitary, Feynman and Landau). For the technical details of the numerical evaluation of the ME and of its integration over the phase space we refer to Ref. [6], as we have adopted here the same procedures.

For the parameters which are in common to the $\mathcal{SM}$ and to the $\mathcal{MSSM}$ we have used the following numerical values: $M_Z = 91.175$ GeV, $\Gamma_Z = 2.5$ GeV, $M_{W^\pm} = M_Z \cos\theta_W \approx 80$ GeV, $\Gamma_{W^\pm} = 2.2$ GeV and $m_b = 4.25$ GeV. For simplicity, we have kept the final state bosons $W^\pm$ on-shell in the computation. The expressions for the $\mathcal{MSSM}$ Higgs mass relations and couplings that we have used are the same that have been summarised in Ref. [17] (see also references therein). The widths of the $\mathcal{MSSM}$ Higgs bosons have been generated by using the `FORTRAN` program described there. In particular, as we have adopted running b-masses in evaluating Γ_H, Γ_h and Γ_A, in order to be consistent, we have used the same $m_b(Q^2 = M^2_\Phi)$ mass also in the $\Phi b\bar{b}$ vertices of the production processes considered here, where $\Phi = H, h$ and A. The values adopted for the strong coupling constant α_s are those at two-loops, for $n_f = 5$ active flavours and $\Lambda^{n_f=5}_{QCD} = 0.13$ GeV, at the scale $Q = \sqrt{s}$, in the $\overline{\mathrm{MS}}$ renormalisation scheme and with $\alpha_s(M_Z) = 0.112$.

As it is clearly impractical to cover all regions of the $\mathcal{MSSM}$ parameter space, we have chosen here, as representative for $\tan\beta$, the two extreme values 1.5 and 30., whereas M_A spans the range 50 to 350 GeV, that is, between the experimental lower limit [18] and the region where the $t\bar{t}$ channels of $\mathcal{MSSM}$ neutral Higgs bosons start dominating the decay phenomenology over a substantial part of the $(M_A, \tan\beta)$ plane [17].

The top width Γ_t has been evaluated according to the formulae given in Ref. [19] (see also Ref. [20]), corrected by means of the expressions of Ref. [21], to account for the $\mathcal{MSSM}$ decay $t \to bH^{\pm}$. In order to obtain results in Narrow Width Approximation (NWA) for the top, we have written the heavy quark propagator as

$$\frac{\not{p} + m_t}{p^2 - m_t^2 + i m_t \Gamma} \left(\frac{\Gamma}{\Gamma_t}\right)^{\frac{1}{2}}. \tag{2}$$

In this way, for $\Gamma = \Gamma_t$ the standard expression is recovered, whereas for $\Gamma \to 0$ one is able to correctly reproduce the rates for $e^+e^- \to t\bar{t}$ times the (squared) branching ratio $[BR(t \to bW^{\pm})]^2$. Numerically, we have used $\Gamma = 10^{-5}$ in NWA.

For the discussion of the results we have assumed the following values for the top mass: $m_t = 170, 172$ and 174 GeV [22] and $m_t = 195, 197$ and 199 GeV [23]. In correspondence, we have taken as CM energy $\sqrt{s} = 350$ and 400 GeV. This has been done in order to perform studies of top-antitop production at threshold, according to the values of m_t measured by CDF and D0, respectively[4]. As top measurements will be certainly performed also far above threshold, we have produced results for the combination $\sqrt{s} = 500$ GeV and $m_t = 174$ and 199 GeV too. The total integrated luminosity assumed for the NLC throughout this paper is $\mathcal{L} = 10$ fb^{-1}. Please also note that in all Tables and Figures the branching ratios of the W's have not been included.

Finally, we are aware that a great number of higher-order results have been presented concerning $t\bar{t}$ production and decay (for a review, see Ref. [25]). For example, QCD correction to the Born cross section up to first order in α_s have been calculated in Ref. [26]. These corrections lead to the familiar Coulomb enhancement at threshold (this also occurs in QED) [27]. The QED-like binding potential between the two top quarks at threshold decreases however rather rapidly [28], such that for $\Delta E \equiv \sqrt{s} - 2m_t \gtrsim 2$ GeV the two fermions behave as free particles and ordinary perturbation theory can be applied (our approach will be indeed to concentrate our attention in this region, referring for the complementary case $\Delta E \lesssim 2$ GeV to more refined studies [27, 28, 29]). EW corrections have been studied in Ref. [30, 31]. These latter are generally negative. Both of them account for an $\mathcal{O}(10\%)$ effect (for $m_t > 170$ GeV). We do not include such corrections here, for two reasons. On the one hand, for consistency, as these are known only for the process $e^+e^- \to t\bar{t} \to b\bar{b}W^+W^-$ but not for the non-resonant background (which is computed here at tree-level only). On the other hand, because the typical

[4]When this work was almost completed the Fermilab Collaborations have both announced new measurements of m_t [24], which seem to shift the top mass towards the lower part of the m_t spectrum considered here. However, as also the new values suffer from rather large uncertainties (such that by summing statistics and systematics the experimental error band would include the most part of top masses that we have chosen), we decided to maintain in the present paper also the part of studies devoted to the case $m_t \approx 199$ GeV.

spikes at threshold due to Coulomb effects are largely smeared out in the excitation curve if the top mass is large, see Ref. [10, 32].

Also concerning the $\mathcal{MSSM}$ Higgs processes $e^+e^- \to ZH$ and $e^+e^- \to AH$ higher-order results have been reported in literature [33, 34]. These are EW corrections, which are generally under control, if the scale of the SUSY partners is set in the TeV region, as we assume here [35, 36]. Again reasons of consistency have induced us to treat Higgs signals and corresponding background in the same way also in this case (i.e., at leading order). The Higgs reaction $e^+e^- \to hW^+W^-$ has been studied within the $\mathcal{SM}$ in Ref. [38], and no higher-order results are known to date.

Beamsstrahlung and Linac energy spread effects [39] have been systematically neglected here, for two reasons. On the one hand, effects due to synchrotron radiation emitted by one of the colliding bunches in the field of the opposite one as well as the intrinsic (to any collider) energy distribution of the beams before annihilation necessarily need, in order to be quantified, the knowledge of the technical details of the collider design and can be realistically estimated only through Monte Carlo simulations. On the other hand, it has been shown that, for narrow beam designs, beamsstrahlung affects the cross section much less than the Initial State Radiation (ISR) [39], such that in phenomenological analyses one can consistently deal with bremsstrahlung radiation only.

Therefore, we will devote some space to discussing the effect of the ISR emitted from electron/positron lines [39]. In particular, we expect the signal $t\bar{t}$ to be quite sensitive at threshold [10]. In this respect, we confine ourselves to some illustrative examples in the presence of ISR, more than implementing this latter in all cases. Both because ISR effects are expected to be qualitatively the same regardless of the actual values of the various parameters ($m_t, \Gamma_t, M_A, \tan\beta$, etc.) and because its inclusion would significantly enhance the CPU time of the runs. In general, however, ISR effects are straightforward to include [40, 41]. The main effect of the ISR is to lower the effective CM energy available in the main process, thus ultimately reducing(enhancing) the total cross sections which increase(decrease) at larger CM energies. Furthermore, ISR also leads to a smearing of the differential distributions [42, 43].

In the very end, in order to perform the foreseen high precision measurements of the top parameters (m_t, Γ_t, τ_t, etc.) and to disentangle Higgs signals at the NLC, a complete phenomenological analysis has to include in full all the above corrections [1]. This is clearly beyond the scope of this study. For the moment, we are mainly concerned with the fact that other aspects so far either ignored (irreducible background in non-top-antitop events) or only approximated in the existing literature (finite width and spin correlation effects in the top production and decay) could be important, such that they must be properly taken into account for a correct analysis, and to check if new Higgs discovery channels could be of experimental interest. To realise whether all of this is true or not, and when, is the final goal of the present paper.

3. Results

In carrying out our analysis we closely follow the approach of Refs. [6, 7], and the phenomenological studies reported in various instances in Ref. [1]. For future reference, we show in Figs. 2a–b the $\mathcal{MSSM}$ mass relations between, on the one hand, the $H^\pm, h$ and H Higgs scalars and, on the other hand, the A pseudoscalar, as well as the partial decay widths of the top quark in the two $\mathcal{MSSM}$ channels $t \to bH^\pm$ and $t \to bW^\pm$, for the mentioned combinations of $\tan\beta$ and M_A.

Throughout this paper, of the two W bosons in the $b\bar{b}W^+W^-$ final state, one is assumed to decay hadronically, $W \to$ jj, and the other leptonically, $W \to \ell\bar{\nu}_\ell$ with $\ell = e, \mu$. This semi-leptonic (or semi-hadronic) final state has a few advantages with respect to the case of two hadronic W decays: it has a simpler topology inside the detectors and thus it is easier to reconstruct; it also allows one to get rid of complications due to the combinatorial in case of a six jet final state. Moreover, like the pure hadronic final state its kinematics is fully constrained (once the missing momentum is assigned to the neutrino). Finally, two leptonic W decays would lead to a double disadvantage: first, a very much reduced statistics and, second, problems in reconstructing invariant mass spectra because of the two neutrinos.

We present our results by treating the top and Higgs production mechanisms in two different Subsections.

3.1 The process $e^+e^- \to t\bar{t} \to (bW^+)(\bar{b}W^-)$

The selection strategies of top-antitop signals we have considered are (see Ref. [32]):

- to perform a scan in $\sqrt{s}$;
- to study the W momentum spectrum;
- to reconstruct the invariant mass of the three-jet system $t \to bW^\pm$.

The first two methods are normally used at threshold ($\sqrt{s} \approx 2m_t$), whereas the last one has been considered for studies far above that ($\sqrt{s} \gg 2m_t$).

In the first method one spans the CM energy in a region of approximately 10 GeV around the real top-antitop threshold, in order to reconstruct the $t\bar{t}$-excitation curve. By using the fit procedures described in Refs. [10, 32] one should be able to measure the top mass as well as to perform a large number of measurements of fundamental quantities, such as the strong coupling constant [27, 28]. Moreover, if m_t and α_s can be measured independently and high experimental precision can be achieved, it may be possible to extract from the data also the values of Γ_t and/or to obtain limits on the mass(es) $M_{\phi(\Phi)}$ and the top Yukawa coupling(s) $\lambda_{\phi(\Phi)}$ of the Higgs boson(s) of the underlying theory [10]. In order to perform a careful analysis, one should include in the end [10]: complete EW corrections to $t\bar{t}$ production [44], higher-order QCD corrections (including 'bound state' and 'short distance' effects) and beam-related phenomena [32, 39].

In the second approach, one exploits the fact that, with the CM energy constraint and after assigning the missing energy and momentum to the neutrino, the W boson four-momentum p_W can be easily reconstructed by adding those of the lepton and of the neutrino, and that the width of the corresponding differential spectrum is sensitive to the top quark mass [32]. Uncertainties due to beam-related effects (ISR, beamsstrahlung) are expected to be generally small, whereas those due to the 'Fermi motion' of the top quarks should be considered in detail in a full simulation [32].

In the third case, one determines m_t from the two three-jet invariant mass distributions ($M_{bW\to 3\mathrm{jet}}$) that can be reconstructed from the $b\bar{b}W^+W^- \to b\bar{b}(\mathrm{jj})(\ell\bar{\nu}_\ell)$ final state, after appropriate selection cuts to reduce the non-top background [32]. In fact, in $b\bar{b}W^+W^-$ events in which one W boson decays hadronically (let us say the W^+) and the other leptonically, there are two possible three-jet combinations among the jj pair reconstructing the W and the two b's[5]: the 'right' one (W^+b), which peaks at m_t, and the 'wrong' one ($W^+\bar{b}$), which gives a rather broad and flat distribution. In this case, systematic errors (which cause a 'top mass shift') are expected from detector and beam-related effects, as well as from top quark fragmentation. However, such a shift can be predicted to high precision [32].

The reason why the first two strategies are usually preferred to the third one at threshold is that for $\sqrt{s} \approx 2m_t$ the top quarks recoil with rather low velocity, such that in the resulting spherical final state the fragments of the top and antitop quarks are mixed up and it is difficult to isolate individual jets and to reconstruct m_t from invariant mass distributions, whereas at higher energies the jets from $t \to bW^\pm \to b(\mathrm{jj})$ decays carry a momentum of a few tens of GeV, which makes it possible to individually recognise them by simply using one of the usual jet finding algorithms [45].

The impact of using a full calculation of $e^+e^- \to b\bar{b}W^+W^-$ events, which includes all the irreducible background, all the finite Γ_t effects as well as all spin correlations between the two top decays in the 'canonical' way, is clear. In fact, in the literature, on the one hand, a complete calculation of non-$t\bar{t}$-resonant events in $b\bar{b}W^+W^-$ final states does not exist to date (within the $\mathcal{MSSM}$) and, on the other hand, it is quite common (especially when one has an 'analytical approach' in mind, see formulae in Ref. [10]) to split the process $e^+e^- \to t\bar{t} \to b\bar{b}W^+W^-$ by separating the $e^+e^- \to t\bar{t}$ production process from the two $t\bar{t} \to b\bar{b}W^+W^-$ decays, considered independently from each other, in the spirit of the so-called 'Narrow Width Approximation'[6]. In particular, with respect to the top search strategies at threshold, we stress two aspects. First, a correct normalisation of the 'underlying' cross section for $b\bar{b}W^+W^-$ events not proceeding via $e^+e^- \to t\bar{t}$ is needed if one wants to disentangle subtle effects due to α_s, to Γ_t and to higher-order contributions of Higgs boson(s), as these can be of the same order as those due to the single-top, the $Z \to b\bar{b}$ [46] and the Higgs [6, 7] production mechanisms in $b\bar{b}W^+W^-$ events. Second, we remind the reader that both the non-$t\bar{t}$-resonant background and the finite value of Γ_t will contribute to smearing out the edges of the p_W spectrum. Concerning the three-jet invariant mass analysis, one has to remember that $e^+e^- \to b\bar{b}W^+W^-$ events that do not proceed via $e^+e^- \to t\bar{t}$ tend to enhance the contribution due to the 'wrong' bW combination, thus reducing the final value of the signal-to-background ratios obtained from the M_{bW} spectrum[7].

In Tabs. I–II we present various cross sections for the three subprocesses

[5]This is true regardless to the fact that one uses or not b-tagging procedures in recognising jets from b-quarks.

[6]Although width and spin correlations effects have been introduced in various instances in previous analyses (see Ref. [10], and references therein).

[7]In addition, although we will not treat this issue here, we notice that a correct inclusion of spin effects between the two top decays is also desirable if one considers that studies of angular correlations of the $t\bar{t}$ decay products are planned at the NLC (the top quark decays before hadronising, such that its original spin polarisation is not washed out by multiple QCD soft radiation), in order to assess or disprove the presence pf CP-violating effects (due to possible 'New Physics') [47, 48, 49].

1. $e^+e^- \to t\bar{t}$ (Narrow Width Approximation, null top width);

2. $e^+e^- \to t\bar{t} \to b\bar{b}W^+W^-$ (production and decay diagram only, finite top width);

3. $e^+e^- \to b\bar{b}W^+W^-$ (all diagrams at tree-level, finite top width).

The combinations of energy and top masses are $\sqrt{s} = 350$ GeV and $m_t = 170, 172, 174$ GeV (Tab. I); $\sqrt{s} = 400$ GeV and $m_t = 195, 197, 199$ GeV (Tab. II). In the upper part of the tables we present rates when no cut is implemented, whereas in the lower part the constraint $M_{\rm had} > 200$ GeV is applied [32], where $M_{\rm had}$ represents the invariant mass of the system $b\bar{b}W^+$, if W^+ is the gauge boson decaying hadronically. The first line refers to $\tan\beta = 1.5$ whereas the second corresponds to numbers obtained by using $\tan\beta = 30$. For each process and combination of masses and energies four cross sections are given, corresponding to $M_A = 60, 140, 220, 300$ GeV (without and inside parentheses, brackets and braces, respectively). As can be seen from Fig. 2b, the partial top width into $bH^\pm$ is zero for $M_A \gtrsim 180$ GeV (both for $\tan\beta = 1.5$ and $\tan\beta = 30.$), such that rates for the processes $t\bar{t}$ and $t\bar{t} \to b\bar{b}W^+W^-$ do not change in the above range of M_A.

We have displayed the cross sections of processes 1.–3. in three different columns, and this allows one to appreciate the effect of the finite width Γ_t and of the irreducible background separately. As already observed in the case of the $\mathcal{SM}$, rates for the process $e^+e^- \to t\bar{t}$ (first column) are larger than those for $e^+e^- \to t\bar{t} \to b\bar{b}W^+W^-$ (second column), both at $\sqrt{s} = 350$ GeV and $\sqrt{s} = 400$ GeV. The effect is clearly due to a value of Γ in the top-antitop propagators (2) which is finite in the second case ($\Gamma = \Gamma_t$), whereas in NWA one has $\Gamma \to 0$. Correspondingly, in the integration over the phase space a Breit-Wigner distribution replaces a delta function. Moreover, in the case of the process $e^+e^- \to t\bar{t} \to b\bar{b}W^+W^-$ there is an additional reduction (which increases with the top width) due to the limited phase space available, as the invariant mass tail of the top-antitop decays at large p^2 in equation (2) can fall outside the kinematical bounds dictated by the CM energy and by the top mass [6]. Such a reduction gets larger with increasing m_t and decreasing M_A, whereas the effect is largely independent of $\tan\beta$ (see Figs. 2a–b). Differences are $\lesssim 13\%$, both at $\sqrt{s} = 350$ and 400 GeV. The corrections due to the irreducible background in $e^+e^- \to b\bar{b}W^+W^-$ events can be estimated by comparing rates in the second and third columns. These are larger as the top mass and the CM energy of the collider increase, since, on the one hand, non-resonant events do not suffer from the threshold effects described above and, on the other hand, they do not have a pure s–channel structure like top-antitop pair production. The maximum effects are $\approx 5\%$ for $m_t = 174$ GeV and $\approx 9\%$ at $m_t = 199$ GeV. In this case there is not a marked dependence on $\tan\beta$.

By comparing the lower part with the upper part of Tabs. I–II one can appreciate the effect of the cut in $M_{\rm had}$, which is indeed rather weak. This fact was already recognized in the case of the $\mathcal{SM}$ [6], when the top mass was large. Not even the increase here of the value adopted for $M_{\rm had}$ counterbalances this fact (in Ref. [32] the cut $M_{\rm had} > 170$ GeV was used, for a top around 140 GeV). The effect is however larger in the case of $e^+e^- \to b\bar{b}W^+W^-$, but only at $\sqrt{s} = 350$ GeV.

The threshold scan in the region $2m_t - 10\ \mathrm{GeV} \le \sqrt{\rm s} - 2\ \mathrm{GeV} \le 2\rm m_t + 10\ GeV$ is performed in Fig. 3a–b, for $m_t = 174$ and 199 GeV, respectively, for three different values of M_A and both $\tan\beta = 1.5$ and 30. From these figures is rather clear how the knowledge of $e^+e^- \rightarrow b\bar{b}W^+W^-$ events that do not proceed through a $t\bar{t}$ resonance is essential is order to correctly estimate the sensitivity of the top excitation curve on m_t, Γ_t, α_s, M_Φ and λ_Φ [32]. In fact, the difference between the curves for the processes $e^+e^- \rightarrow t\bar{t} \rightarrow b\bar{b}W^+W^-$ and $e^+e^- \rightarrow b\bar{b}W^+W^-$ in Figs. 3a–b can be large below threshold. However, the knowledge of the rates for the two above processes allows one to perform a 'subtraction' between the dashed(dotted) and continuous(chain-dotted) curves of Figs. 3a–b, thus extracting the effect due to the irreducible background from the experimental samples which will be used in the analyses. We also notice that for $m_t = 174$ GeV the cross sections below threshold are smaller than those for $m_t = 199$ GeV, whereas above threshold it is the other way round: that is, the curves in Fig. 3a are steeper than those in Fig. 3b. Figs. 3c–d show the same rates when the ISR is included (we have used the formulae given in Ref. [41]). Here, cross sections are smaller by several tens of percent than those in Figs. 3a–b, with rates slightly more suppressed when $\sqrt{s} \approx 2m_t$.

Other than on the integrated rates, finite width and irreducible background effects are (strikingly) visible in the spectrum of the W boson three-momentum, both at $\sqrt{s} = 350$ and 400 GeV, and for all top masses considered here. Figs. 4a–b report the distributions in case of the NWA (at the bottom) and of the complete set of diagrams in $e^+e^- \rightarrow b\bar{b}W^+W^-$ events (two top plots), for $M_A = 100$ and 260 GeV and the following values of top masses: $m_t = 170, 174$ GeV (Fig. 4a) and $m_t = 195, 199$ GeV (Fig. 4b). As the shape of the distributions does not substantially change by varying $\tan\beta$, for convenience we present here rates for the case $\tan\beta = 1.5$ only. The kinematic bounds on the p_W distribution that would stick out rather clearly in the case of the $e^+e^- \rightarrow t\bar{t}$ process in NWA and would allow one to reconstruct m_t, are largely smeared out once Γ_t and background effects are properly included. This is especially true for $m_t = 174$ and 199 GeV. Thus, extreme care is needed in such analyses, together with an accurate knowledge of the above effects around the edges of the p_W spectrum, if one wants to achieve high precision measurements.

The strong variations of the p_W spectrum with the top mass are also a reflection of its dependence on the fundamental parameters of the $\mathcal{MSSM}$, as can be seen from Figs. 5a–b (and again from Figs. 2a–b). Here, the same distribution as in Figs. 4a–b is plotted, but for the case of the complete $e^+e^- \rightarrow b\bar{b}W^+W^-$ process, and for different values of M_A (with m_t fixed at 174 and 199 GeV, in Fig. 5a and 5b, respectively). For the same reasons as above, we plot here distributions for only one of the two values of $\tan\beta$ that we have chosen (for example, $\tan\beta = 30.$ now). The same sort of trend would also be visible in the cases $m_t = 170, 172$ and 195, 197 GeV. The normalisation of the various curves is rather different, according to the numbers given in Tabs. I–II and depending on the value of M_A, when the latter is less than ≈ 180 GeV (compare to Figs. 4a–b too). For $M_A \gtrsim 180$ GeV there is a clear 'degeneracy' between the different curves, reflecting the fact, on the one hand, that the value of Γ_t does not change in this interval and, on the other hand, that the differences due to the different contributions of the Higgs processes to the total cross section are rather small (compared to $e^+e^- \rightarrow t\bar{t}$). It is however clear that any possible deviation from the shapes and normalizations of the cross sections predicted by the $\mathcal{MSSM}$ (at fixed M_A and $\tan\beta$) can easily be tested by studying the p_W spectrum.

As explained in the Introduction, top studies at the NLC will also be performed far above threshold. Thus, we report in Tab. III the cross sections for processes 1.–3. at $\sqrt{s} = 500$ GeV, assuming for the top mass the two values $m_t = 174$ and 199 GeV (in this energy regime there is practically no dependence on m_t if this changes by 2 or 4 GeV). The selection of Higgs masses in Tab. III is the same as in the two previous ones, as well as the organisation of the rates depending on M_A, $\tan\beta$ and on the cuts. Since the suppression of the high invariant masses of the bW pairs does not act any longer, finite width effects above threshold are fairly small, of a few percent only. In some instances these are even completely negligible: for example, for $m_t = 174$ GeV. Irreducible background effects are around 5% at the most, generally for all combinations of m_t, M_A and $\tan\beta$. The cut implemented here is $0.95 \le x_E \le 1.05$, where $x_E = E_{bW\to 3\mathrm{jet}}/E_{\mathrm{beam}}$, again according to the analysis of Ref. [32]. This constraint is somewhat more effective that the one used at threshold, as it reduces the $e^+e^- \to b\bar{b}W^+W^-$ rates by more than twice the $e^+e^- \to t\bar{t} \to b\bar{b}W^+W^-$ ones (by approximately 5% the former and by 2% the latter).

Above threshold one can extract the value of the top mass from a fit to the observed invariant mass distributions of the three-jet systems bW^+ (the 'right' one) and $\bar{b}W^+$ (the 'wrong' one). Figs. 6a–b show such spectra for $\sqrt{s} = 500$ GeV, $m_t = 174$ and 199 GeV, $M_A = 100$ and 260 GeV, and for $\tan\beta = 1.5$ (Fig. 6a) and $\tan\beta = 30$. (Fig. 6b). As can be seen clearly, the $\bar{b}W^+$ distribution is generally well below the bW^+ one around m_t, by more than one order of magnitude. One should notice however that the bins in Figs. 6a–b are 2 GeV wide, when the experimental resolutions (in energy and angle) on the hadronic system constituted by the three jets will probably be worse than that, such that Figs. 6a–b represent a sort of 'benchmark' result of the data analyses. For example, an experimental resolution in $M_{3\mathrm{jet}}$ of only (let us say) 10 GeV would correspond to lowering the bW^+ peaks in Figs. 6a–b by a factor of five, leaving the spectrum in $\bar{b}W^+$ unchanged.

3.2 The processes $e^+e^- \to ZH \to (b\bar{b})(W^+W^-)$, $e^+e^- \to AH \to (b\bar{b})(W^+W^-)$ and $e^+e^- \to hW^+W^- \to (b\bar{b})W^+W^-$

The neutral Higgs bosons of the $\mathcal{MSSM}$ can be produced primarily at the NLC via

$$\text{bremsstrahlung}: \quad \mathrm{e^+e^- \to (Z^*) \to Z\Phi}; \tag{3}$$

$$\text{pair production}: \quad \mathrm{e^+e^- \to (Z^*) \to A\Phi}; \tag{4}$$

$$WW\text{−fusion}: \quad \mathrm{e^+e^- \to \nu_e\bar{\nu}_e(W^*W^*) \to \nu_e\bar{\nu}_e\Phi}; \tag{5}$$

$$ZZ\text{−fusion}: \quad \mathrm{e^+e^- \to e^+e^-(Z^*Z^*) \to e^+e^-\Phi}; \tag{6}$$

where here $\Phi = h$ and H[8]. Simple expressions relate their cross sections to those of the bremsstrahlung and vector-vector fusion processes of the $\mathcal{SM}$ [36]. Updated and detailed theoretical [14, 42, 43] (also at the complete one-loop level [33]) and experimental [37] analyses making use of the above processes are available in the literature. In general, the first two mechanisms dominate over the last two at smaller CM energies ($\sqrt{s} \approx 300 - 500$ GeV), whereas at $\sqrt{s} \gtrsim 500$ GeV WW-fusion has bigger rates if the Φ

[8]The pseudoscalar boson A does not couple at leading order to the gauge bosons W and Z.

mass is less than ≈ 160 GeV. In general, the cross section for ZZ-fusion is about one order of magnitude smaller than that for WW-fusion. Furthermore, from the results of Ref. [38], one deduces that sizeable rates should be expected for events of

$$\text{Higgs production with two W bosons :} \qquad \mathrm{e^+e^- \to hW^+W^-}, \tag{7}$$

especially at small value of M_h and $\tan\beta$ [50].

By studying $e^+e^- \to b\bar{b}W^+W^-$ events one implicitly considers the first two processes (3)–(4) and the last one (7), in which $h, A, Z \to b\bar{b}$ and $H \to W^+W^-$[9]. As we are concerned here with final-state W bosons produced on-shell, we are forced to ignore the off-shell decays $h, H \to W^*W^*$ (that is, when $M_{h,H} < 2M_W$). However, the below-threshold channel W^*W^* is unlikely to be particularly relevant in experimental analyses. In the case of the light neutral Higgs the corresponding BR is either too small (at small $\tan\beta$) or is sizable only over a very narrow portion of the $\mathcal{MSSM}$ parameter space (at large $\tan\beta$). In the case of the heavy neutral Higgs, the decay $H \to W^*W^*$ is overwhelmed by $H \to hh$ below the $2M_W$ threshold for $\tan\beta = 1.5$, whereas for $\tan\beta = 30$. it is always smaller than $H \to hh, AA$ as well as $H \to b\bar{b}, \tau^+\tau^-$, in the relevant off-shell range. The on-shell decay $H \to WW$ is certainly of interest for small values of $\tan\beta$, as it dominates over the range 160 GeV $\lesssim M_H \lesssim$ 200 GeV and has the second highest BR after the hh channel from $M_A \approx 200$ GeV up to the opening of the threshold for the decay $H \to t\bar{t}$. We do not expect any sizable $H \to WW$ signal if $\tan\beta$ is on the contrary very large [17].

Concerning the $b\bar{b}$ decays of the Z, h and A bosons, we stress two aspects. On the one hand, the same arguments which led us in the Introduction to count the $Z \to b\bar{b}$ decay mode among the cleanest Z signatures in the $\mathcal{SM}$ at the NLC are certainly still valid within the $\mathcal{MSSM}$. On the other hand, the $h, A \to b\bar{b}$ decay channels largely dominate the decay spectrum of the two Higgs scalars: in fact, the $BR(h \to b\bar{b})$ is the largest for all values of M_A and $\tan\beta$ whereas the $BR(A \to b\bar{b})$ is overcome by that of other channels only at small $\tan\beta$'s and for $M_A \gtrsim 200$ GeV [17]. Moreover, we would like to stress that in the W^+W^- semi-leptonic decay mode we do not expect complications due the jet combinatorics, because, first, excellent b-tagging performances are expected at the NLC [8] and, second, b-decays of the W bosons are prohibited by the top mass $m_t > M_W$ and the Cabibbo-Kobayashi-Maskawa mixing matrix.

Among the various search strategies that can be adopted at the NLC in order to detect such Higgs signals [1] we consider here the following two:

- the 'missing mass' analysis;
- the 'direct reconstruction' method.

They are both described in Ref. [51], in the case of the $\mathcal{SM}$; however, these procedures are useful also in the case of the $\mathcal{MSSM}$. In this context, in the first case one studies the invariant mass recoiling against the Z and A bosons tagged via the $b\bar{b}$ pair, by means of the relation $M^2_{\mathrm{recoil}} = [(p_{e^+} + p_{e^-}) - (p_b + p_{\bar{b}})]^2$, whereas in the second case one reconstructs Higgs peaks by computing the resonant invariant mass directly from

[9] Also other Higgs production mechanisms take place in the whole of the process $e^+e^- \to b\bar{b}W^+W^-$ (see graphs 20–21 & 27 in Refs. [6, 7]): these are however very much suppressed.

the four-momenta of the decay products of the scalar bosons [42, 43][10]. Thus, both procedures are applicable to processes (3)–(4), whereas in case of process (7) only the second is exploitable.

Our results concerning Higgs physics in $e^+e^- \rightarrow b\bar{b}W^+W^-$ events are summarised in Figs. 7–11. As already announced, Higgs rates are expected to be larger at smaller $\tan\beta$ values, for all the processes (3)–(4) and (7). Therefore, we will treat the case $\tan\beta = 1.5$ only.

As explained in Ref. [7], looking at the plane $(M_{b\bar{b}}, M_{W^+W^-})$ one realises that, whereas Higgs signals tend to concentrate in single clusters whose size is determined in the end by the experimental reconstruction uncertainties, on the contrary, background events (mostly from $t\bar{t}$ production and decay) tend to fill a rather large kinematical region. In Fig. 7 we show the boundaries of the double differential distribution $d\sigma/dM_{b\bar{b}}/dM_{W^+W^-}$ in the plane $(M_{b\bar{b}}, M_{W^+W^-})$ in the case of $e^+e^- \rightarrow t\bar{t}$ in NWA, for all the combinations of $\sqrt{s}$ and m_t that we have adopted in our study, without any sort of cuts[11].

As outlined in Refs. [7], it is then possible, for a given m_t, to find values of the $\mathcal{MSSM}$ neutral Higgs masses for which the two double differential distributions (of Higgs and top events) do not overlap. In these cases the latter can be very simply distinguished from the former and detecting the Higgs scalars is only a matter of event rate, whereas when the $M_{b\bar{b}}$ and/or $M_{W^+W^-}$ spectra overlap, more refined studies are necessary. Furthermore, from Fig. 7 it also clear that it should be easier in principle to detect Higgs signals when the CM energy of the collider is set around the $2m_t$ threshold, more than when the former is far beyond the latter. In fact, first, rates for $e^+e^- \rightarrow t\bar{t}$ are smaller at threshold that at $\sqrt{s} = 500$ GeV and, second, the regions in the $(M_{b\bar{b}}, M_{W^+W^-})$ plane occupied by $t\bar{t}$ production and decay are more narrow (at fixed m_t). Therefore, to some extent, a collider energy configuration primarily designed for top studies at threshold (i.e., $\Delta E \rightarrow 0$) would also improve the chances of successful Higgs searches in the $b\bar{b}W^+W^-$ channel.

As an example of the various possible cases we study here the combinations ($\tan\beta = 1.5$):

1. $\sqrt{s} = 350$ GeV, $m_t = 174$ GeV and $M_A = 140, 180$ GeV;
2. $\sqrt{s} = 400$ GeV, $m_t = 199$ GeV and $M_A = 140, 180$ GeV;
3. $\sqrt{s} = 400$ GeV, $m_t = 199$ GeV and $M_A = 60, 100, 220, 260, 300, 340$ GeV;
4. $\sqrt{s} = 500$ GeV, $m_t = 199$ GeV and $M_A = 60, 100$ GeV.

In cases 1. and 2. the Higgs peaks are right next to the maxima of the $t\bar{t}$ distributions in both the $M_{b\bar{b}}$ and $M_{W^+W^-}$ spectra (Figs. 8–9). For the first combination the following Higgs peaks are expected: $h \rightarrow b\bar{b}$ at $M_{b\bar{b}} \approx 80(93)$ and $86(102)$ GeV, corresponding to $m_t = 174(199)$ GeV; $A \rightarrow b\bar{b}$ at $M_{b\bar{b}} \approx 140$ and 180 GeV; $H \rightarrow W^+W^-$ at

[10]In our 'partonic' analysis (where no detector effect and experimental efficiencies are considered) the two spectra in M_{recoil} and M_{WW} necessarily coincide.

[11]The dependence of such regions on the actual value of Γ_t (thus on the $\mathcal{MSSM}$ parameters) in eq. (2), when $\Gamma \rightarrow 0$, is completely negligible. Rates in Fig. 7 have been plotted for $M_A = 100$ GeV and $\tan\beta = 1.5$.

$M_{W^+W^-} \approx 182(195)$ and $212(222)$ GeV, again corresponding to $m_t = 174(199)$ GeV. The $Z \to b\bar{b}$ resonance gives indirect evidence of process (3) with $\Phi = h$, yet many of the non-Higgs diagrams proceed through a Z decay into $b\bar{b}$ pairs, such that the two normalisations (of signal and background events) need to be carefully known in order to make Higgs detection feasible in such a case. The combination of CM energy and top/Higgs masses where the rewards for Higgs searches are largest is the second. In this case Higgs peaks in the $b\bar{b}$ spectrum are already visible before any selection cut is applied, apart from the cases: $M_h \approx 93$ GeV (which is degenerate with the Z peak) and $M_A \approx 180$ GeV (overwhelmed by the $t\bar{t}$ background), Fig. 8b (main plot). On the contrary, for the combination in 1. it is generally impossible to disentangle Higgs resonances from the pure total cross sections before cuts, Fig. 8a (main plot). These conclusions depend largely on the invariant mass resolutions, however, it has to be observed that bins in the main windows of Fig. 8–9 are large, 5 GeV (a value, in our opinion, which is not too distant from the performances experimentally achievable). Of course, if the precision in the angular and energy measurements is higher (resulting, let us say, in a mass resolution around 1 GeV), all the above decay phenomenology in $b\bar{b}$ events can be covered in principle (small windows in Figs. 8a–b), with special attention devoted to the case of h/Z mass degeneracy. In the case of the H resonance in the $M_{W^+W^-}$ spectrum things are less optimistic (Figs. 9a–b, main windows), apart from the case $M_H \approx 195$ GeV (at $\sqrt{s} = 400$ GeV, for $M_A = 140$ GeV). Therefore, in order to disentangle $H \to W^+W^-$ resonances, one generally needs to apply Higgs selection cuts. For example, by requiring that in events for which $|M_{b\bar{b}} - M_{Z,A}| < 10$ GeV one of the W's fails to reproduce the kinematics of a $t\bar{t}$ final state when coupled with either of the two b's (namely that $m_t - 10 \text{ GeV} > |M_{W^+b(W^+\bar{b})}| > m_t + 10$ GeV and $E_{\text{beam}} - 10 \text{ GeV} > |E_{W^+} + E_{b(\bar{b})}| > E_{\text{beam}} + 10$ GeV), one obtains the results displayed in the two small insertions on the right of Figs. 9a–b. That is, to recognise H signals in W^+W^- decays one needs both to apply selection cuts to reduce the top-antitop background and to achieve high invariant mass resolutions to resolve the peaks (unless M_H is around 195 GeV when $M_A = 140$ GeV and the CM energy is 400 GeV). Furthermore, it is clear that once similar cuts are applied to the $M_{b\bar{b}}$ spectrum, all the decay phenomenology for $h, A \to b\bar{b}$ should be exploited easily.

From the rates given in Figs. 8 one can generally extract about ten Higgs events per year with rather little background. On the contrary, from the numbers in Figs. 9 (when $M_H \not\approx 195$ GeV), one is able to detect Higgs signals only after several years of running and if the collider yearly luminosity is of the order of 100 fb^{-1}. It should also be noticed that in the case of the $H \to W^+W^-$ decay the application of Higgs selection cuts reduces even further the total rates. Finally , one has to ultimately consider that the semi-leptonic signature $W^+W^- \to (\text{jj})(\ell\bar{\nu}_\ell)$, with $\ell = e, \mu$, introduces a reduction factor equal to the product of the $BR(W \to \text{jj}) \approx 70\%$ and the $BR(W \to \ell\bar{\nu}_\ell) \approx 20\%$: actually, times 2, because of the two combinations in which the W's can decay semi-leptonically.

The combination in 3. corresponds to the case in which the $h, A \to b\bar{b}$ peaks are either on the tail of the top-antitop distribution in $M_{b\bar{b}}$ (Fig. 10, upper window) or rather far from the Z resonance such that problems of mass degeneracy should be avoided (Fig. 10, two lower windows). Chances of h and A detection are convincing (more at smaller than at larger values of M_A), provided that good invariant mass resolutions can be achieved (distributions in Fig. 10 are plotted in bins of 1 GeV). For these combinations of CM energy and top masses $H \to W^+W^-$ signals can be disentangled only if $M_A \lesssim 100$ GeV, for which M_H is close enough to the $2M_W$ threshold, such that the BR into two W's is large (the pattern is rather similar to that illustrated for $M_A = 140$ GeV). For $M_A \gtrsim 220$ GeV the H boson is very heavy (i.e., $M_H \gtrsim 250$ GeV) compared to the available CM energy at threshold, and so the corresponding cross section is kinematically suppressed.

Fig. 11 shows what happens to the $M_{W^+W^-}$ spectrum for the combination of masses in 4., with the collider energy well above the $t\bar{t}$ threshold (contrary to the previous three cases). Here, even when no selection cut is applied, H signals are visible, again especially at small values of M_A (i.e., for M_H rather close to the $2M_W$ threshold). The $H \to W^+W^-$ peaks, in fact, occur in Fig. 11 at $M_{W^+W^-} \approx 165$ and 176 GeV. In this case then, the chances of heavy neutral Higgs detection are larger, thanks especially to the fact that the region delimited by 60 GeV $\lesssim \mathrm{M_{b\bar{b}}} \lesssim$ 100 GeV and $M_{W^+W^-}$ between the above two values is practically free from the background due to $e^+e^- \to t\bar{t}$ events (see Fig. 7).

4. Conclusions

In this paper we have studied the process

$$e^+e^- \to b\bar{b}W^+W^-$$

within the $\mathcal{MSSM}$, at NLC energies ($\sqrt{s} = 350, 400$ and 500 GeV), for the following values of the parameters of the model: 60 GeV $\lesssim \mathrm{M_A} \lesssim$ 340 GeV and $\tan\beta = 1.5, 30$. In our calculation, all the Feynman diagrams contributing at tree-level to the above reaction have been considered, with no approximations.

This process is phenomenologically extremely interesting, as it includes among the various contributions to the total cross section the following subprocesses:

$$e^+e^- \to t\bar{t} \to (bW^+)(\bar{b}W^-),$$

$$e^+e^- \to ZH \to (b\bar{b})(W^+W^-),$$
$$e^+e^- \to AH \to (b\bar{b})(W^+W^-),$$
$$e^+e^- \to hW^+W^- \to (b\bar{b})W^+W^-,$$

where H, h and A represent the neutral Higgs bosons of the $\mathcal{MSSM}$, as well the contributions of non-resonant diagrams (irreducible background). For the top mass, the following values have been adopted: $m_t = 170, 172$ and 174 GeV (when $\sqrt{s} = 350$ GeV) and $m_t = 195, 197$ and 199 GeV (when $\sqrt{s} = 400$ GeV). At $\sqrt{s} = 500$ GeV the two values $m_t = 174$ and 199 GeV have been considered. Our results are applicable to all energies excluding a narrow window of a few GeV at threshold.

Final states of the type $b\bar{b}W^+W^-$ are decisive in both top and Higgs processes. On the one hand, top pairs produced via the process $e^+e^- \to t\bar{t}$ decay through $t\bar{t} \to (bW^+)(\bar{b}W^-)$ over most of the $\mathcal{MSSM}$ parameter space $(M_A, \tan\beta)$. On the other hand, the $b\bar{b}$ decay channel might well be one of best ways to detect the Z gauge boson and represents the most accessible signature of the Higgs scalars h and A (thanks to the corresponding high BRs and to the excellent performance in tagging jets originating from b-quarks now foreseen for the vertex devices which will be installed at the NLC). Moreover, the decay channel $H \to W^+W^-$ of the heaviest of the $\mathcal{MSSM}$ Higgs scalars is dominant over a sizable part of the M_H range, for small $\tan\beta$'s.

Phenomenological analyses have been carried out, in order to quantify, first, the influence of finite top width and irreducible background effects on the integrated and differential rates as obtained from $e^+e^- \to t\bar{t}$ events in Narrow Width Approximation and, second, to establish the detectability of the Higgs processes, as a function of the values assumed by the fundamental parameters of the $\mathcal{MSSM}$.

Although before drawing any firm conclusion from our results, these should be folded with a realistic simulation of the expected performances of the NLC detectors, they clearly indicate that the finite width of the top and the irreducible background can have a significant impact on the measurement of the parameters of the top, both near and above the $\sqrt{s} = 2m_t$ threshold. Furthermore, in a number of cases (especially at small M_A's and $\tan\beta$'s), it should be possible to disentangle Higgs resonances, the $h, A \to b\bar{b}$ channels being easier to detect than the $H \to W^+W^-$ one.

Throughout our analysis we have considered the $W^+W^- \to (\mathrm{jj})(\ell\bar{\nu}_\ell)$ signature of the gauge bosons (with $\ell = e, \mu$), and assumed high b- and lepton tagging efficiency, such that all the background to the mentioned top and Higgs events can be ascribed to the irreducible one.

The effect of Initial State Radiation has been analysed in a few cases.

Finally, a similar study of the pure $\mathcal{MSSM}$ processes

$$e^+e^- \to b\bar{b}W^+H^-$$

and

$$e^+e^- \to b\bar{b}H^+H^-$$

is now in progress [52].

5. Acknowledgements

We thank Bryan Webber for reading the manuscript. This work is supported in part by the Ministero dell' Università e della Ricerca Scientifica, the UK PPARC, and the EC Programme "Human Capital and Mobility", Network "Physics at High Energy Colliders", contract CHRX-CT93-0357 (DG 12 COMA).

References

[1] Proceedings of the Workshop "e^+e^- *Collisions at 500 GeV. The Physics Potential* ", Munich, Annecy, Hamburg, 3–4 February 1991, ed. P.M. Zerwas, DESY 92–123A/B, August 1992, DESY 93–123C, December 1993.

[2] Proceedings of the Workshop on "*Physics at Current Accelerators and Supercolliders* ", eds. J. Hewett, A. White and D. Zeppenfeld, Argonne National Laboratory, 1993.

[3] G. Altarelli, T. Sjöstrand and F. Zwirner, eds., '*Report of the Workshop on Physics at LEP2*', CERN 96–01 (1996).

[4] CMS Technical Proposal, CERN/LHC/94-43 LHCC/P1, December 1994.

[5] ATLAS Technical Proposal, CERN/LHC/94-43 LHCC/P2, December 1994.

[6] A. Ballestrero, E. Maina and S. Moretti, *Phys. Lett.* **B333** (1994) 434.

[7] A. Ballestrero, E. Maina and S. Moretti, *Phys. Lett.* **B335** (1994) 460.

[8] Proceedings of the Workshop on "*High Luminosities at LEP* ", CERN Report 91-02, Geneva, Switzerland.

[9] J. Guasch and J. Solà, *preprint* UAB-FT-389, March 1996.

[10] W. Bernreuther *et al.*, in Ref. [1], part A.

[11] C.S. Li and T.C. Yuan, *Phys. Rev.* **D42** (1990) 3088.

[12] A. Denner, R.J. Guth and J.H. Kühn, *Nucl. Phys.* **B377** (1992) 3.

[13] A. Djouadi, J. Kalinowski and P.M. Zerwas, in Ref. [1], part A.

[14] A. Djouadi, J. Kalinowski and P.M. Zerwas, in Ref. [1], part A (and references therein).

[15] A. Ballestrero and E. Maina, *Phys. Lett.* **B350** (1995) 225.

[16] K. Hagiwara and D. Zeppenfeld, *Nucl. Phys.* **B274** (1986) 1.

[17] S. Moretti and W.J. Stirling, *Phys. Lett.* **B347** (1995) 291; Erratum, *ibidem* **B366** (1996) 451.

[18] See for example:
D. Treille, in Proceedings of the Workshop on "*Physics and Experiments with Linear* e^+e^- *Colliders* ", Waikoloa, Hawaii, 1993, eds. F. Harris *et al.*, Vol. I (and references therein).

[19] R. Kleiss and W.J. Stirling, *Z. Phys.* **C40** (1988) 419.

[20] I. Bigi, Y. Dokshitzer, V.A. Khoze, J. Kühn and P.M. Zerwas, *Phys. Lett.* **B181** (1986) 157.

[21] G.L. Kane, Proceedings of the "*Madison Workshop* " (1979).

[22] CDF Collaboration, *Phys. Rev. Lett.* **74** (1995) 2626.

[23] D0 Collaboration, *Phys. Rev. Lett.* **74** (1995) 2632.

[24] A. Caner, Presented at "*Rencontres du Physique de la Valle d'Aoste*", March 1996; M. Narain, Presented at the '*Rencontres du Physique de la Valle d'Aoste*", March 1996.

[25] M. Jeżabek and J.H. Kühn, *preprint* TTP-93-4, February 1993.

[26] J. Jersak, E. Laermann and P.M. Zerwas, *Phys. Rev.* **D25** (1982) 363;
J. Schwinger, "Particles, Sources and Fields" (Addison-Wesley, Reading MA, 1973);
L. Reinders, H. Rubinstein and S. Yazaki, *Phys. Rep.* **C127** (1985) 1;
S. Güsken, J.H. Kühn and P.M. Zerwas, *Phys. Lett.* **B155** (1985) 185.

[27] V.S. Fadin and V.A. Khoze, *JETP Lett.* **46** (1987) 525; *Sov. J. Nucl. Phys.* **53** (1988) 692.

[28] M.J. Strassler and M.E. Peskin, *Phys. Rev.* **D43** (1991) 1500.

[29] V.S. Fadin and O.I. Yakovlev, *Sov. J. Nucl. Phys.* **23** (1991) 1117;
M. Jeżabek, J.H. Kühn and T. Teubner, *Z. Phys.* **C56** (1992) 653;
Y. Sumino, K. Fujii, K. Hagiwara, H. Murayama and C.-K. Ng, *Phys. Rev.* **D47** (1992) 56;
M. Jeżabek and T. Teubner, *Z. Phys.* **C59** (1993) 669.

[30] A. Denner and T. Sack, *Nucl. Phys.* **B348** (1991) 46;
W. Beenakker, S.C. van der Marck and W. Hollik, *Nucl. Phys.* **B365** (1991) 24.

[31] V. Driesen, W. Hollik and A. Kraft, *preprint* KA-TP-1996, March 1996, to appear in Proceedings of the Workshop "*Physics with e^+e^- Colliders* ", Annecy, Gran Sasso, Hamburg, 1995.

[32] G. Bagliesi *et al.*, in Ref. [1], part A.

[33] P. Chankowski, S. Pokorski and J. Rosiek, *Phys. Lett.* **B274** (1992) 191; *Phys. Lett.* **B286** (1993) 307; *Nucl. Phys.* **B423** (1994) 437 and 497;
J. Rosiek, A. Sopczak, P. Chankowski and S. Pokorski, in Ref. [1], part C.

[34] A. Dabelstein and W. Hollik, in Ref. [1], part C.

[35] M. Böhm, A. Denner, T. Sack, W. Beenakker, F.A. Berends and H. Kuijf, *Nucl. Phys.* **B304** (1988) 463;
J. Fleisher F. Jegerlehner and M. Zralek, *Z. Phys.* **C42** (1989) 409.

[36] J.F. Gunion, L. Roszkowski, A. Turski, H. Haber, G. Gamberini, B. Kayser, S. Novaes, F. Olness and J. Wudka, *Phys. Rev.* **D38** (1988) 3444.

[37] P. Janot, in Ref. [1], part A (and references therein).

[38] V. Barger, T. Han and A. Stange, *Phys. Rev.* **D42** (1990) 777;
M. Baillargeon, F. Boudjema, F. Cuypers, E. Gabrielli and B. Mele, in Ref. [1], part C.

[39] T. Barklow, P. Chen and W. Kozanecki, in Ref. [1], part A.

[40] F.A. Berends, W.L. van Neerven and G.J. Burgers, *Nucl. Phys.* **B297** (1988) 429; Erratum, *ibidem* **B304** (1988) 95;
E.A. Kuraev and V.S. Fadin, *Sov. J. Nucl. Phys.* **41** (1985) 466;
G. Altarelli and G. Martinelli, Proceedings of the Workshop '*Physics at LEP*', eds. J. Ellis and R. Peccei, Gèneva, 1986, CERN 86-02;
R. Kleiss, *Nucl. Phys.* **B347** (1990) 29.

[41] O. Nicrosini and L. Trentadue, *Phys. Lett.* **B196** (1987) 551; *Z. Phys.* **C39** (1988) 479.

[42] V. Barger, K. Cheung, A. Djouadi, B.A. Kniehl and P.M. Zerwas, *Phys. Rev.* **D49** (1994) 79.

[43] V. Barger, K. Cheung, A. Djouadi, B.A. Kniehl, R.J.N. Phillips and P.M. Zerwas, in Ref. [1], part C.

[44] R.J. Guth and J.H. Kühn, *Nucl. Phys.* **B368** (1992) 38.

[45] S. Bethke, Z. Kunszt, D.E. Soper and W.J. Stirling, *Nucl. Phys.* **B370** (1992) 310.

[46] A. Ballestrero, V.A. Khoze, E. Maina, S. Moretti and W.J. Stirling, *preprint* DFTT 03/95, DTP/95/08, Cavendish–HEP–95/14, October 1995 (to be published in *Z. Phys.* **C**).

[47] J.F. Donoghue and G. Valencia, *Phys. Rev. Lett.* **58** (1987) 451; Erratum, *ibidem* **60** (1988) 243;
W. Bernreuther, U. Löw, J.P. Ma and O. Nachtmann, *Z. Phys.* **C43** (1989) 117;
W. Bernreuther and O. Nachtmann, *Phys. Lett.* **B268** (1991) 424;
C.A. Nelson, *Phys. Rev.* **D41** (1990) 2805;
G.L. Kane, G.A. Ladinsky and C.P. Yuan, *Phys. Rev.* **D45** (1992) 124.

[48] M. Jeżabek and J.H. Kühn, *Phys. Lett.* **B329** (1994) 317.

[49] S. Jadach and J.H. Kühn, *preprint* MPI-PAE/PTh-64/86, October 1986.

[50] J.F. Gunion, H.E. Haber, G.L. Kane and S. Dawson, "The Higgs Hunter Guide" (Addison-Wesley, Reading MA, 1990).

[51] P. Grosse-Wiesmann, D. Haidt and H.J. Schreiber, in Ref. [1], part A.

[52] S. Moretti, in preparation.

Table Captions

Tab. I Cross sections in femtobarns for $e^+e^- \rightarrow t\bar{t}$ (Narrow Width Approximation, $\Gamma \rightarrow 0$), for $e^+e^- \rightarrow t\bar{t} \rightarrow b\bar{b}W^+W^-$ (production and decay diagram only, $\Gamma = \Gamma_t$) and for $e^+e^- \rightarrow b\bar{b}W^+W^-$ (all diagrams at tree-level, $\Gamma = \Gamma_t$), within the $\mathcal{MSSM}$, at $\sqrt{s} = 350$ GeV, for $m_t = 170, 172$ and 174 GeV, and $M_A = 60(140)[220]\{300\}$ GeV. The upper part refers to rates obtained when no cut is applied, the lower one to rates obtained when the cut $M_{\rm had} > 200$ GeV is implemented. The first(second) row reports rates for $\tan\beta = 1.5(30.)$.

Tab. II Same as in Tab. I, at $\sqrt{s} = 400$ GeV, for $m_t = 195, 197$ and 199 GeV.

Tab. III Cross sections in femtobarns for $e^+e^- \rightarrow t\bar{t}$ (Narrow Width Approximation, $\Gamma \rightarrow 0$), for $e^+e^- \rightarrow t\bar{t} \rightarrow b\bar{b}W^+W^-$ (production and decay diagram only, $\Gamma = \Gamma_t$) and for $e^+e^- \rightarrow b\bar{b}W^+W^-$ (all diagrams at tree-level, $\Gamma = \Gamma_t$), within the $\mathcal{MSSM}$, at $\sqrt{s} = 500$ GeV, for $m_t = 174$ and 199 GeV, and $M_A = 60(140)[220]\{300\}$ GeV. The upper part refers to rates obtained when no cut is applied, the lower one to rates obtained when the cut $0.95 \leq x_E \leq 1.05$ is implemented. The first(second) row reports rates for $\tan\beta = 1.5(30.)$.

Figure Captions

Fig. 1 The $\mathcal{MSSM}$ Feynman graph contributing in lowest order to $e^+e^- \rightarrow (Ah), (AH) \rightarrow b\bar{b}W^+W^-$. The dashed line connected to the $b\bar{b}$ one represents the A scalar, whereas the other refers to both a h and a H boson. The other 27 $\mathcal{SM}$-like topologies of Feynman graphs contributing in lowest order to the complete ME for $e^+e^- \rightarrow b\bar{b}W^+W^-$ in the $\mathcal{MSSM}$ can be found in Refs. [6, 7], where a dashed line represents both a h and a H boson.

Fig. 2 $\mathcal{MSSM}$ mass relations of the charged $H^\pm$ and of the neutral h and H Higgs bosons with respect to the pseudoscalar neutral one A, for $\tan\beta = 1.5$ and 30., for different values of the top mass (**a**), and partial decay widths of the top quark in the channels $t \rightarrow bH^\pm$ and $t \rightarrow bW^\pm$ within the $\mathcal{MSSM}$, as a function of M_A, for $\tan\beta = 1.5$ and 30., and different values of top masses (**b**). Continuous and dotted lines in **a** coincide, as we have used here the tree-level relation for the charged Higgs mass. The dashed and chain-dotted curves corresponding to the $h(H)$ boson are those extending to the right lower(upper) corner in **a**.

Fig. 3 Cross section in femtobarns for $e^+e^- \rightarrow b\bar{b}W^+W^-$ events around the top-antitop threshold, for two different values of M_A: (**a**) $\sqrt{s} = 350$ GeV and $m_t = 174$ GeV; (**b**) $\sqrt{s} = 400$ GeV and $m_t = 199$ GeV; Continuous lines: $\tan\beta = 1.5$ and production and decay diagram only. Dashed lines: $\tan\beta = 1.5$ and all diagrams. Dotted lines: $\tan\beta = 30.$ and production and decay diagram only. Chain-dotted lines: $\tan\beta = 30.$ and all diagrams. In all cases $\Gamma = \Gamma_t$ has been used. In (**c**) and (**d**) the same as above, but in the presence of ISR. Continuous and dotted lines coincide for $M_A \gtrsim 180$ GeV.

Fig. 4 Differential distributions in the momentum of the W boson, in $e^+e^- \rightarrow b\bar{b}W^+W^-$ events, within the $\mathcal{MSSM}$, in the cases: Narrow Width Approximation for $M_A = 100$ and 260 GeV (lower windows), all diagrams for $M_A = 100$ GeV (upper windows) and $M_A = 260$ GeV (middle windows), with $\tan\beta = 1.5$. The CM energies and the top masses are: (**a**) $\sqrt{s} = 350$ GeV and $m_t = 170, 174$ GeV; (**b**) $\sqrt{s} = 400$ GeV and $m_t = 195, 199$ GeV. Continuous and dotted lines: $m_t = 170(195)$ GeV. Dashed and chain-dotted lines: $m_t = 174(199)$ GeV. The cut in hadronic mass $M_{\mathrm{had}} > 200$ GeV is negligible in all plots.

Fig. 5 Differential distributions in the momentum of the W boson, in $e^+e^- \rightarrow b\bar{b}W^+W^-$ events, within the $\mathcal{MSSM}$, for a selection of pseudoscalar Higgs masses, with $\tan\beta = 30.$ All diagrams are here considered. The CM mass energies and top masses are: (**a**) $\sqrt{s} = 350$ GeV and $m_t = 174$ GeV; (**b**) $\sqrt{s} = 400$ GeV and $m_t = 199$ GeV. No cut has been applied.

Fig. 6 Differential distributions in the invariant mass of the 'right' and 'wrong' three-jet combinations (see the text), in $e^+e^- \rightarrow b\bar{b}W^+W^-$ events, within the $\mathcal{MSSM}$, for $M_A = 100$ (upper window) and 260 (lower window) GeV, with $\tan\beta = 1.5$ (**a**) and 30. (**b**). All diagrams have been here considered. The CM energy is $\sqrt{s} = 500$ GeV. Continuous lines: $m_t = 174$ GeV. Dotted lines: $m_t = 199$ GeV. No cut has been applied.

Fig. 7 The boundaries of the double differential distributions $d\sigma/dM_{b\bar{b}}/dM_{W^+W^-}$ in the plane $(M_{b\bar{b}}, M_{W^+W^-})$ for $e^+e^- \to t\bar{t}$ events in NWA, at $\sqrt{s} = 350, 400$ and 500 GeV, for different values of m_t. No cut has been applied here.

Fig. 8 Differential distributions in invariant mass of the $b\bar{b}$ pair, in $e^+e^- \to b\bar{b}W^+W^-$ events, within the $\mathcal{MSSM}$, for $\tan\beta = 1.5$ GeV and two different values of M_A. CM energies and top masses are: $\sqrt{s} = 350$ GeV and $m_t = 174$ GeV (**a**); $\sqrt{s} = 400$ GeV and $m_t = 199$ GeV (**b**). Continuous lines: all $e^+e^- \to b\bar{b}W^+W^-$ diagrams, with $M_A = 140$ GeV. Dashed lines: all $e^+e^- \to b\bar{b}W^+W^-$ diagrams, with $M_A = 180$ GeV. The two small windows on the right show the regions around the h and Z resonances enlarged and plotted with high resolution, together with the $t\bar{t}$ contribution in NWA (shaded). The small central window in **b** does the same for the A resonance, at $M_{b\bar{b}} = 140$ GeV. No cut has been applied here.

Fig. 9 Differential distributions in invariant mass of the W^+W^- pair, in $e^+e^- \to b\bar{b}W^+W^-$ events, within the $\mathcal{MSSM}$, for $\tan\beta = 1.5$ GeV and two different values of M_A. CM energies and top masses are: $\sqrt{s} = 350$ GeV and $m_t = 174$ GeV (**a**); $\sqrt{s} = 400$ GeV and $m_t = 199$ GeV (**b**). In the two small windows the regions around the H resonances are enlarged and plotted with high resolution, together with the $t\bar{t}$ contribution in NWA (shaded). Continuous lines: all $e^+e^- \to b\bar{b}W^+W^-$ diagrams, with $M_A = 140$ GeV. Dashed lines: all $e^+e^- \to b\bar{b}W^+W^-$ diagrams, with $M_A = 180$ GeV. In the large window no cut is applied, whereas in the two small ones the following constraints have been implemented: $m_t - 10$ GeV $> |M_{W^+b(W^+\bar{b})}| > m_t + 10$ GeV and $E_{\mathrm{beam}} - 10$ GeV $> |E_{W^+} + E_{b(\bar{b})}| > E_{\mathrm{beam}} + 10$ GeV, $|M_{b\bar{b}} - M_{Z,A}| < 10$ GeV.

Fig. 10 Differential distributions in invariant mass of the $b\bar{b}$ pair, in $e^+e^- \to b\bar{b}W^+W^-$ events, within the $\mathcal{MSSM}$, for $\tan\beta = 1.5$ GeV and six different values of M_A. CM energies and top masses are: $\sqrt{s} = 400$ GeV and $m_t = 199$ GeV. The shaded areas correspond to the $t\bar{t}$ contribution in NWA: in the top window the dotted(black) region refers to $M_A = 100(60)$ GeV, whereas in the central(lower) window the shaded regions refer to $M_A = 220, 260(300, 340)$ GeV. All diagrams have been considered in the resonant contributions. No cut has been applied here.

Fig. 11 Differential distributions in invariant mass of the W^+W^- pair, in $e^+e^- \to b\bar{b}W^+W^-$ events, within the $\mathcal{MSSM}$, for $\tan\beta = 1.5$ GeV and two different values of M_A. CM energies and top masses are: $\sqrt{s} = 500$ GeV and $m_t = 199$ GeV. The shaded areas correspond to the $t\bar{t}$ contribution in NWA. All diagrams have been considered in the resonant contributions. No cut has been applied here.

m_t (GeV)	$\sigma(e^+e^- \rightarrow X)$ (fb)		
	$t\bar{t}$	$t\bar{t} \rightarrow \bar{b}bW^+W^-$	$\bar{b}bW^+W^-$
170	341(503)[508]{508} 311(502)[508]{508}	314(470)[475]{475} 286(469)[475]{475}	322(481)[484]{484} 292(479)[484]{484}
172	264(390)[396]{396} 243(389)[396]{396}	237(357)[362]{362} 217(355)[362]{362}	244(366)[371]{374} 224(363)[370]{370}
174	152(225)[230]{230} 141(224)[230]{230}	134(200)[204]{204} 124(199)[204]{204}	141(210)[213]{214} 130(207)[212]{212}
no cut			
170	341(503)[508]{508} 311(502)[508]{508}	312(467)[472]{472} 283(466)[472]{472}	318(476)[479]{479} 289(474)[479]{479}
172	264(390)[396]{396} 243(389)[396]{396}	235(355)[360]{360} 215(353)[360]{360}	241(362)[367]{370} 221(360)[366]{366}
174	152(225)[230]{230} 141(224)[230]{230}	132(199)[203]{203} 123(198)[203]{203}	136(207)[210]{210} 127(204)[209]{209}
$M_{\rm had} > 200$ GeV			
$\sqrt{s} = 350$ GeV			

Tab. I

m_t (GeV)	$\sigma(e^+e^- \rightarrow X)$ (fb)		
	$t\bar{t}$	$t\bar{t} \rightarrow \bar{b}bW^+W^-$	$\bar{b}bW^+W^-$
195	227(329)[362]{362}	201(298)[329]{329}	214(311)[340]{340}
	231(331)[362]{362}	204(299)[329]{329}	213(311)[340]{340}
197	176(254)[282]{282}	151(224)[249]{249}	164(235)[261]{261}
	180(256)[282]{282}	155(225)[249]{249}	164(238)[260]{261}
199	102(147)[164]{164}	89(129)[145]{145}	101(144)[156]{155}
	105(148)[164]{164}	92(130)[145]{145}	101(142)[155]{156}
no cut			
195	227(329)[362]{362}	200(297)[328]{328}	213(310)[339]{339}
	231(331)[362]{362}	204(299)[329]{329}	212(310)[339]{339}
197	176(254)[282]{282}	150(223)[249]{249}	163(234)[260]{260}
	180(256)[282]{282}	154(224)[249]{249}	163(237)[259]{260}
199	102(147)[164]{164}	89(129)[145]{145}	100(143)[155]{154}
	105(148)[164]{164}	92(130)[145]{145}	100(141)[154]{155}
$M_{\rm had} > 200$ GeV			
$\sqrt{s} = 400$ GeV			

Tab. II

m_t (GeV)	$\sigma(e^+e^- \to X)$ (fb)		
	$t\bar{t}$	$t\bar{t} \to \bar{b}bW^+W^-$	$\bar{b}bW^+W^-$
174	463(684)[698]{698}	463(684)[698]{698}	486(716)[725]{725}
	429(682)[698]{698}	429(681)[698]{698}	451(713)[727]{727}
199	372(537)[600]{600}	365(518)[591]{591}	386(549)[611]{611}
	385(541)[600]{600}	377(532)[591]{591}	395(555)[613]{611}
no cut			
174	463(684)[698]{698}	452(671)[685]{685}	462(685)[696]{697}
	429(681)[698]{698}	419(669)[685]{685}	428(683)[698]{698}
199	372(537)[600]{600}	354(516)[577]{577}	365(527)[588]{588}
	385(541)[600]{600}	366(520)[577]{577}	375(531)[588]{588}
$0.95 \leq x_E \leq 1.05$			
$\sqrt{s} = 500$ GeV			

Tab. III

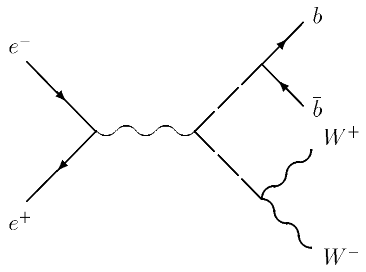

Fig. 1

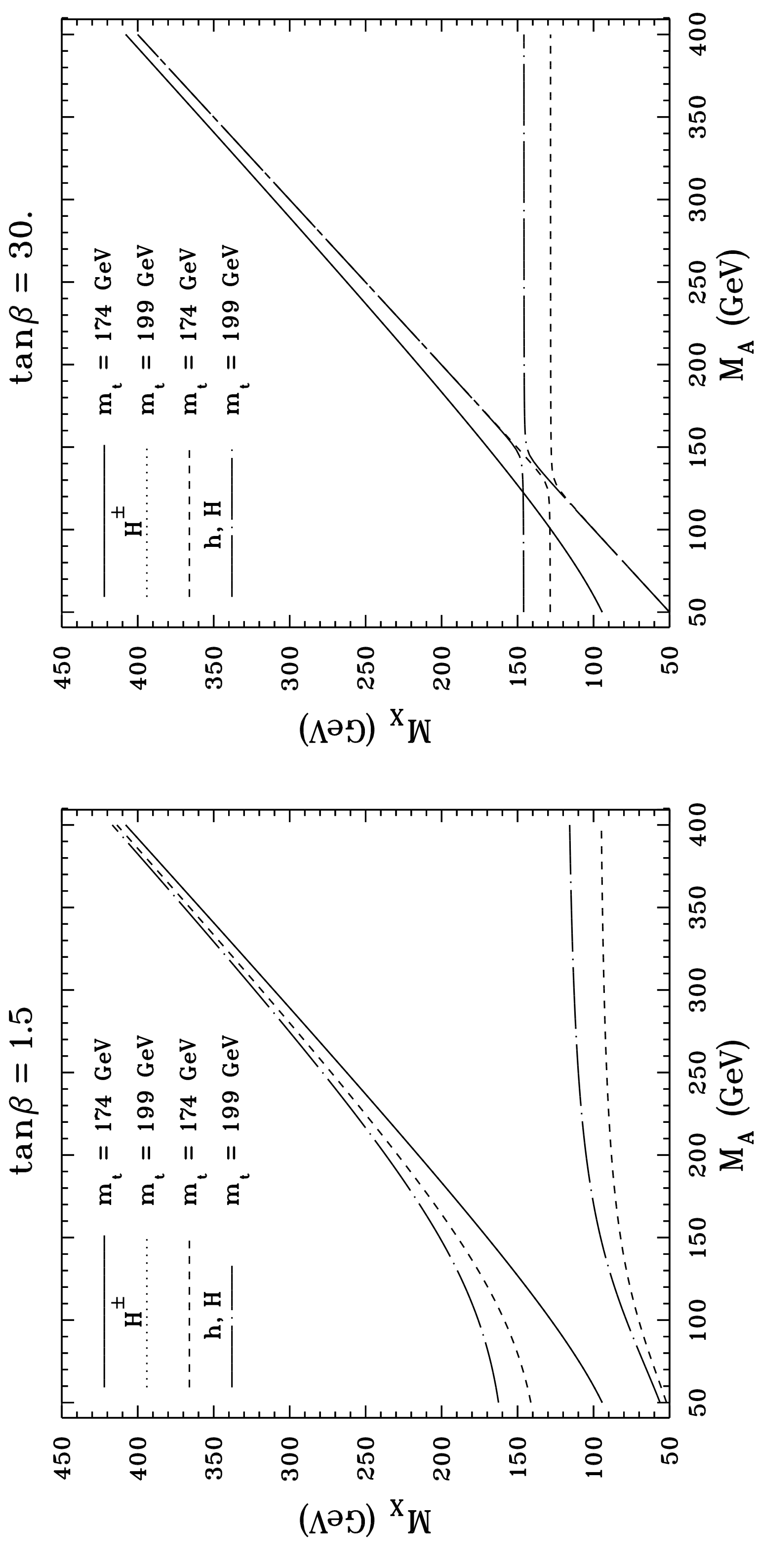

$\tan\beta = 30.$
$\tan\beta = 1.5$
$H^{\pm}$
h, H
m_t = 174 GeV
m_t = 199 GeV
m_t = 174 GeV
m_t = 199 GeV
M_X (GeV)
M_A (GeV)
450
400
350
300
250
200
150
100
50

Fig. 2a

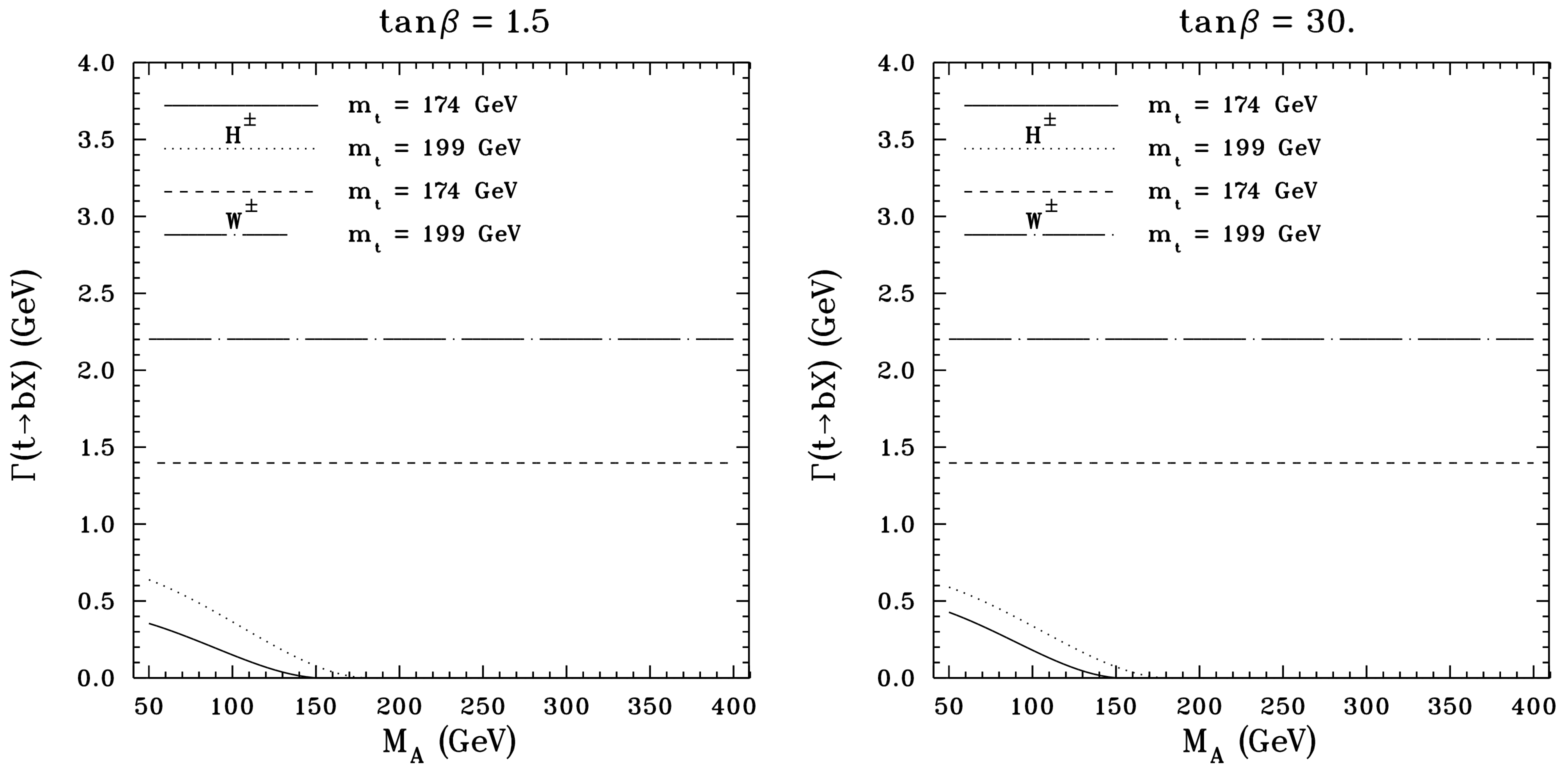

tanβ = 1.5
tanβ = 30.
H±
W±
m t = 174 GeV
m t = 199 GeV
m t = 174 GeV
m t = 199 GeV
Γ(t→bX) (GeV)
M A (GeV)
4.0
3.5
3.0
2.5
2.0
1.5
1.0
0.5
0.0
50
100
150
200
250
300
350
400

Fig. 2b

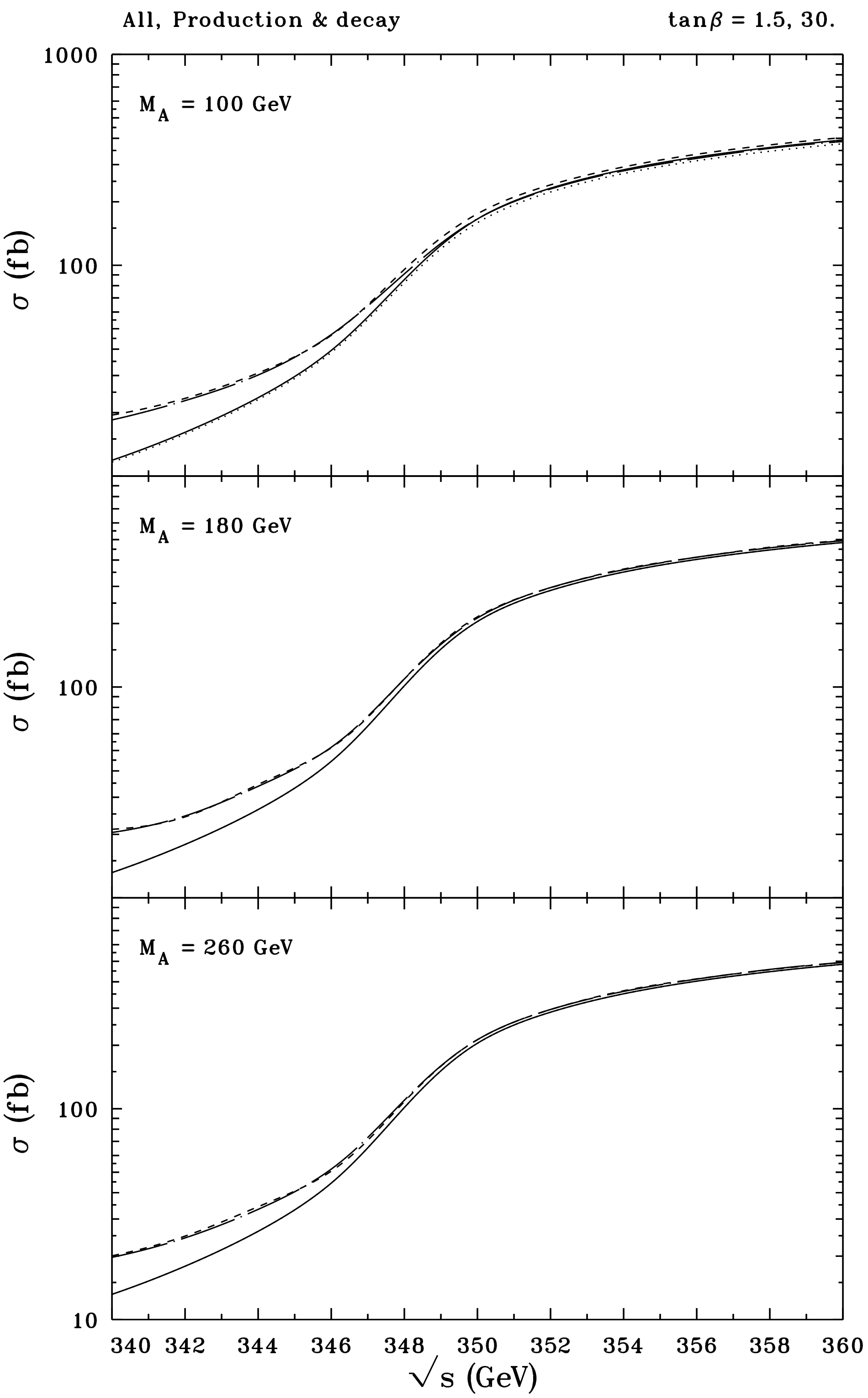

All, Production & decay
tanβ = 1.5, 30.
1000
100
10
σ (fb)
M_A = 100 GeV
M_A = 180 GeV
M_A = 260 GeV
340 342 344 346 348 350 352 354 356 358 360
√s (GeV)

Fig. 3a

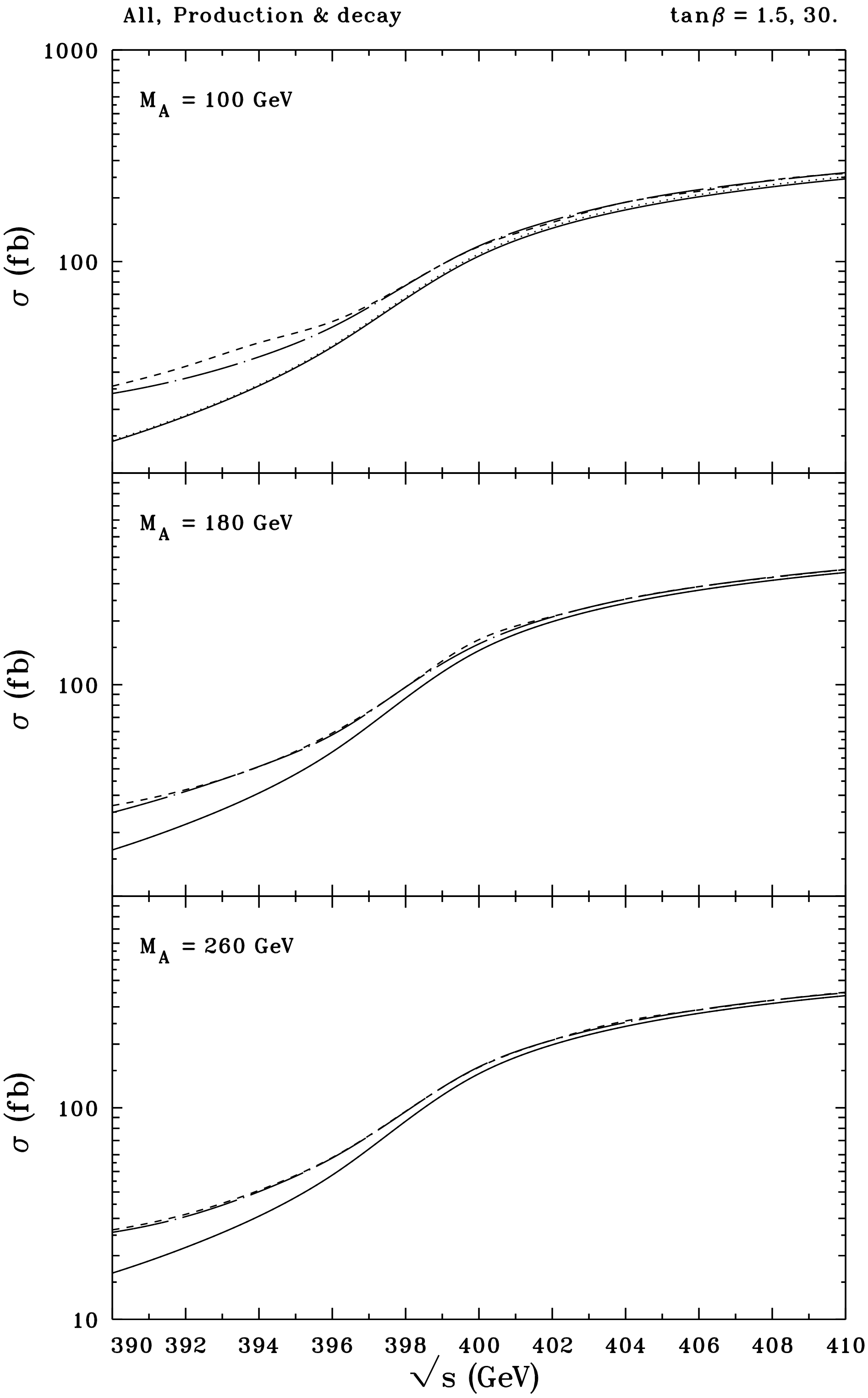
All, Production & decay
tanβ = 1.5, 30.
1000
100
10
M_A = 100 GeV
M_A = 180 GeV
M_A = 260 GeV
σ (fb)
σ (fb)
σ (fb)
390
392
394
396
398
400
402
404
406
408
410
√s (GeV)

Fig. 3b

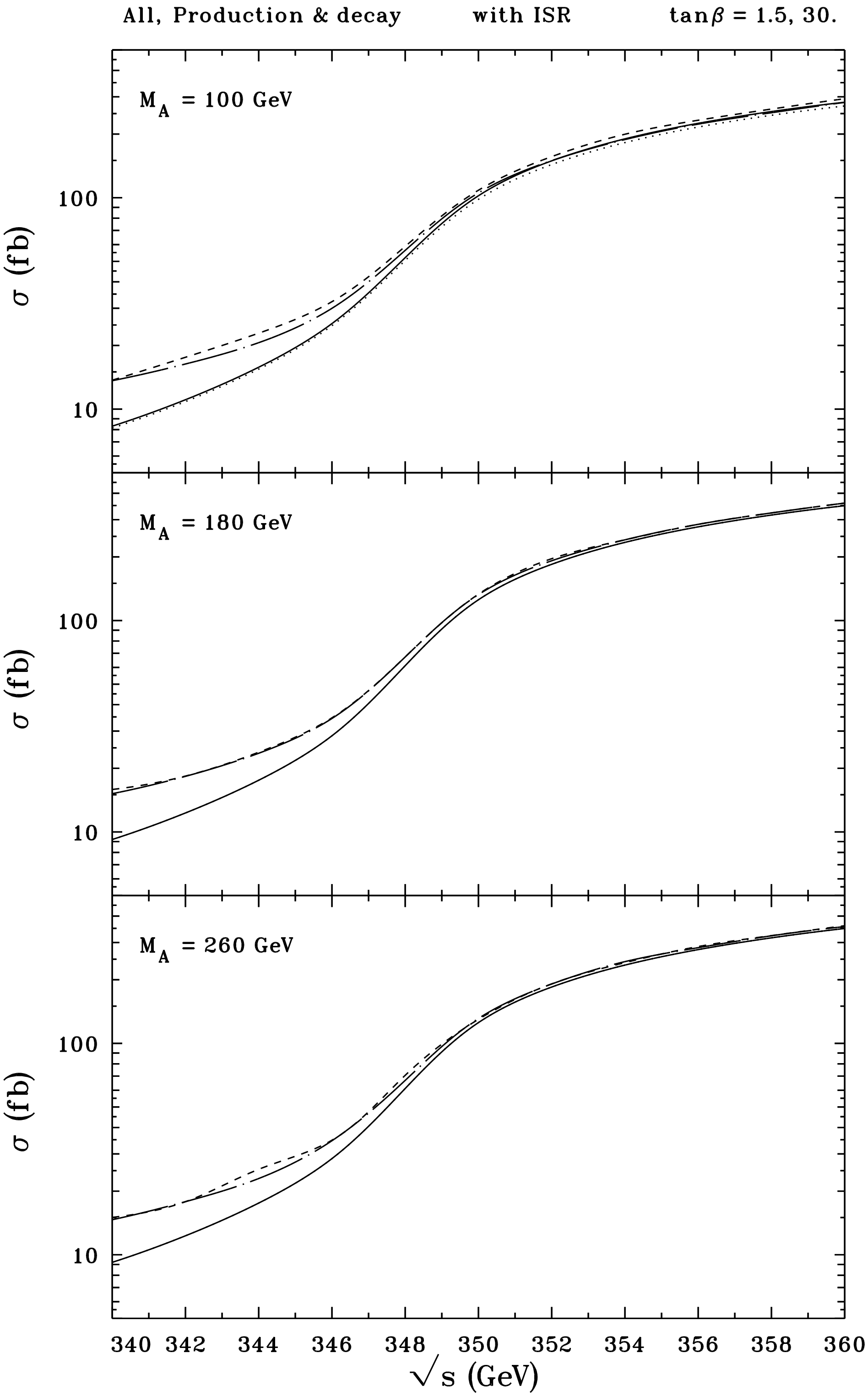
All, Production & decay
with ISR
tanβ = 1.5, 30.
M_A = 100 GeV
M_A = 180 GeV
M_A = 260 GeV
σ (fb)
100
10
340 342 344 346 348 350 352 354 356 358 360
√s (GeV)

Fig. 3c

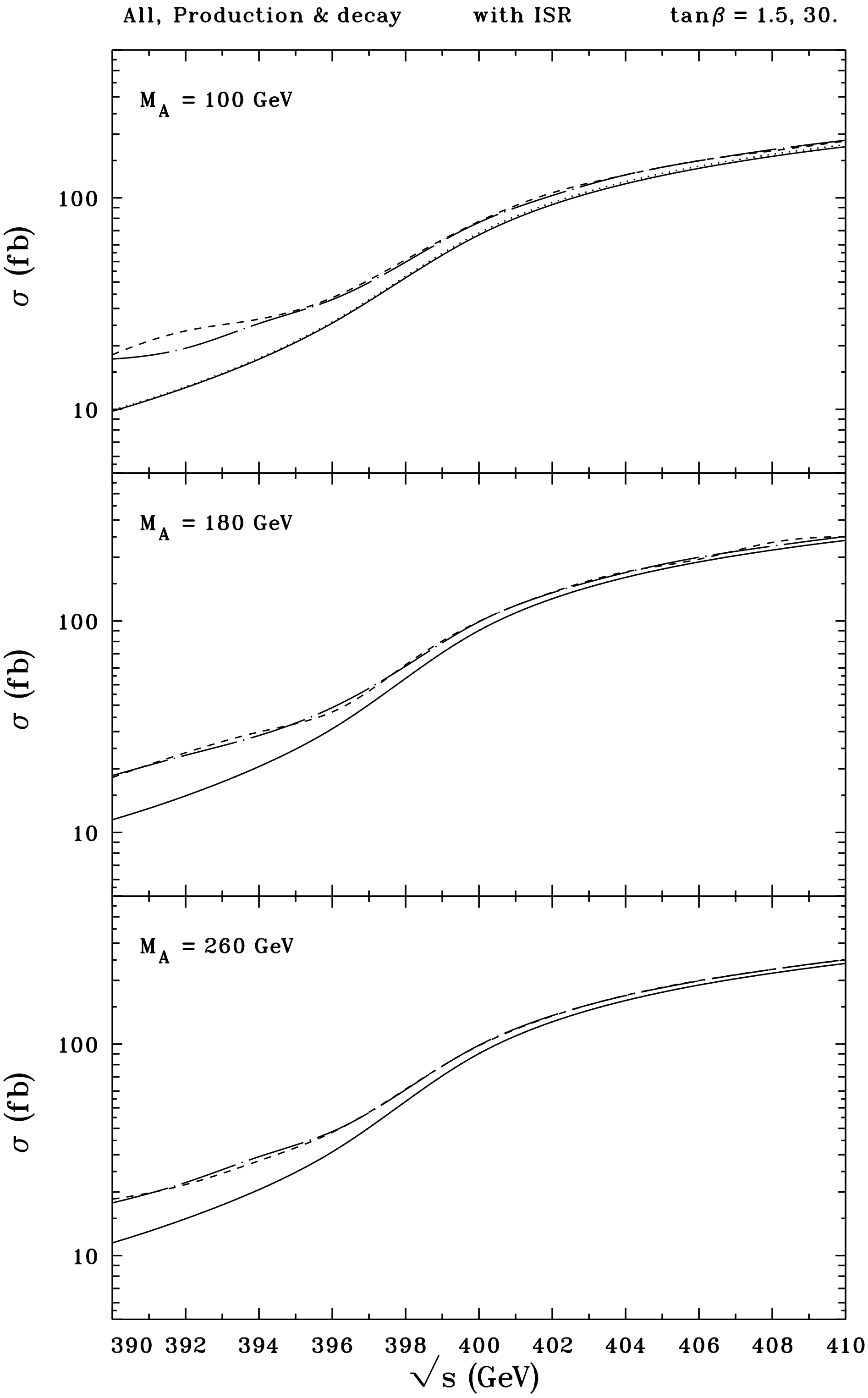
All, Production & decay
with ISR
tanβ = 1.5, 30.
M_A = 100 GeV
M_A = 180 GeV
M_A = 260 GeV
σ (fb)
100
10
390 392 394 396 398 400 402 404 406 408 410
√s (GeV)

Fig. 3d

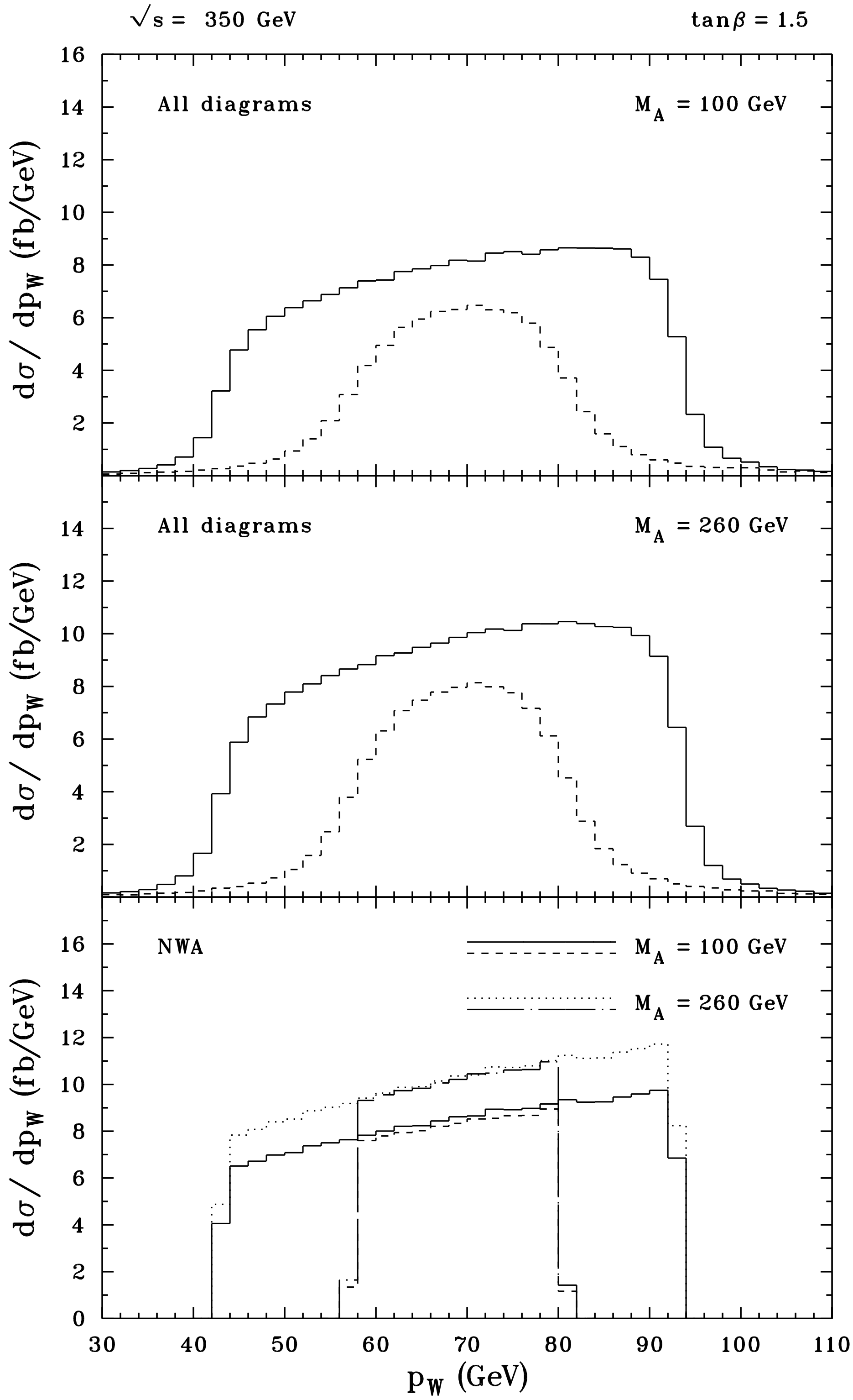

√s = 350 GeV
tanβ = 1.5
All diagrams
M_A = 100 GeV
All diagrams
M_A = 260 GeV
NWA
M_A = 100 GeV
M_A = 260 GeV
dσ/ dp_W (fb/GeV)
p_W (GeV)

Fig. 4a

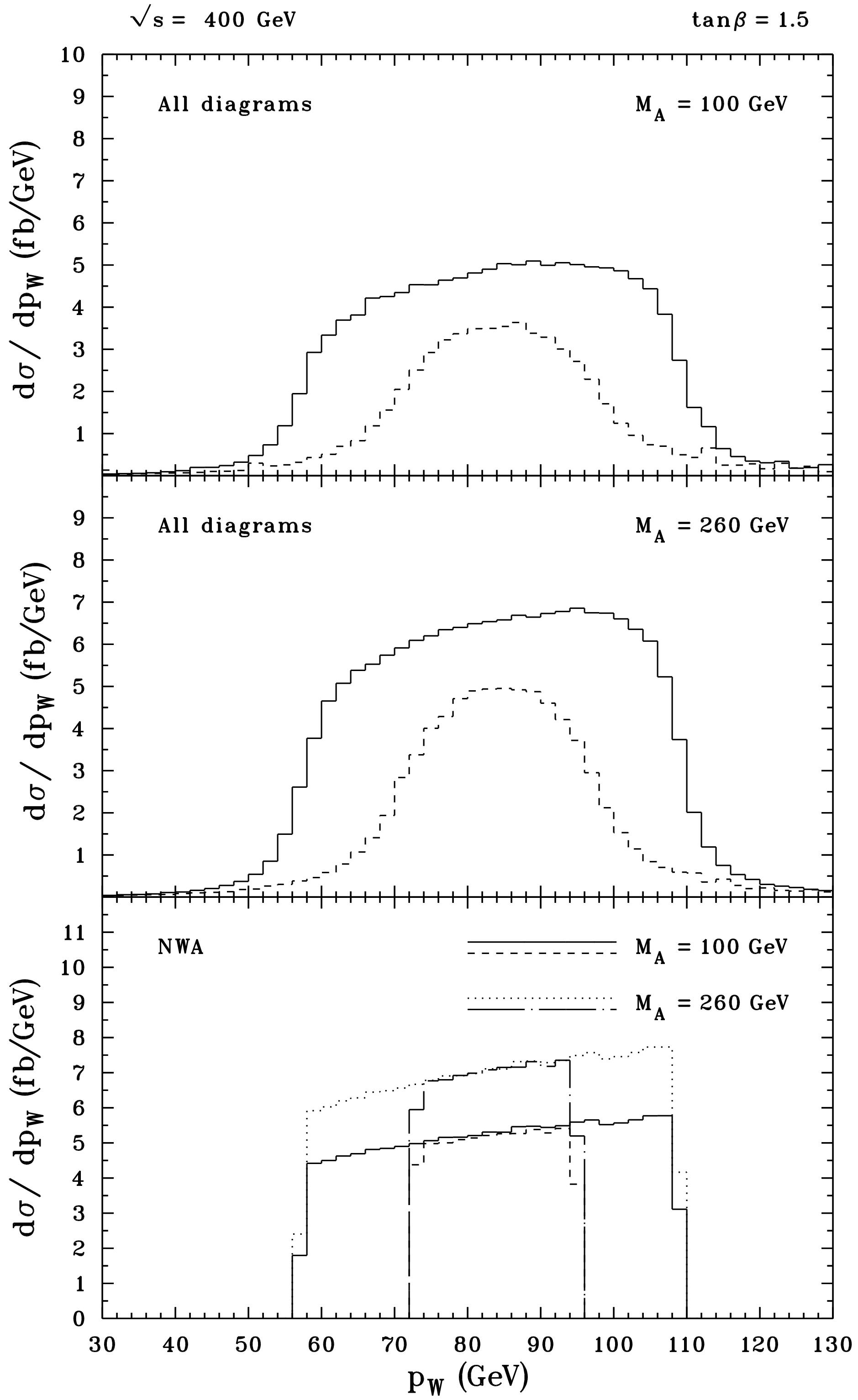

√s = 400 GeV
tanβ = 1.5
All diagrams
M_A = 100 GeV
All diagrams
M_A = 260 GeV
NWA
M_A = 100 GeV
M_A = 260 GeV
dσ/ dp_W (fb/GeV)
p_W (GeV)

Fig. 4b

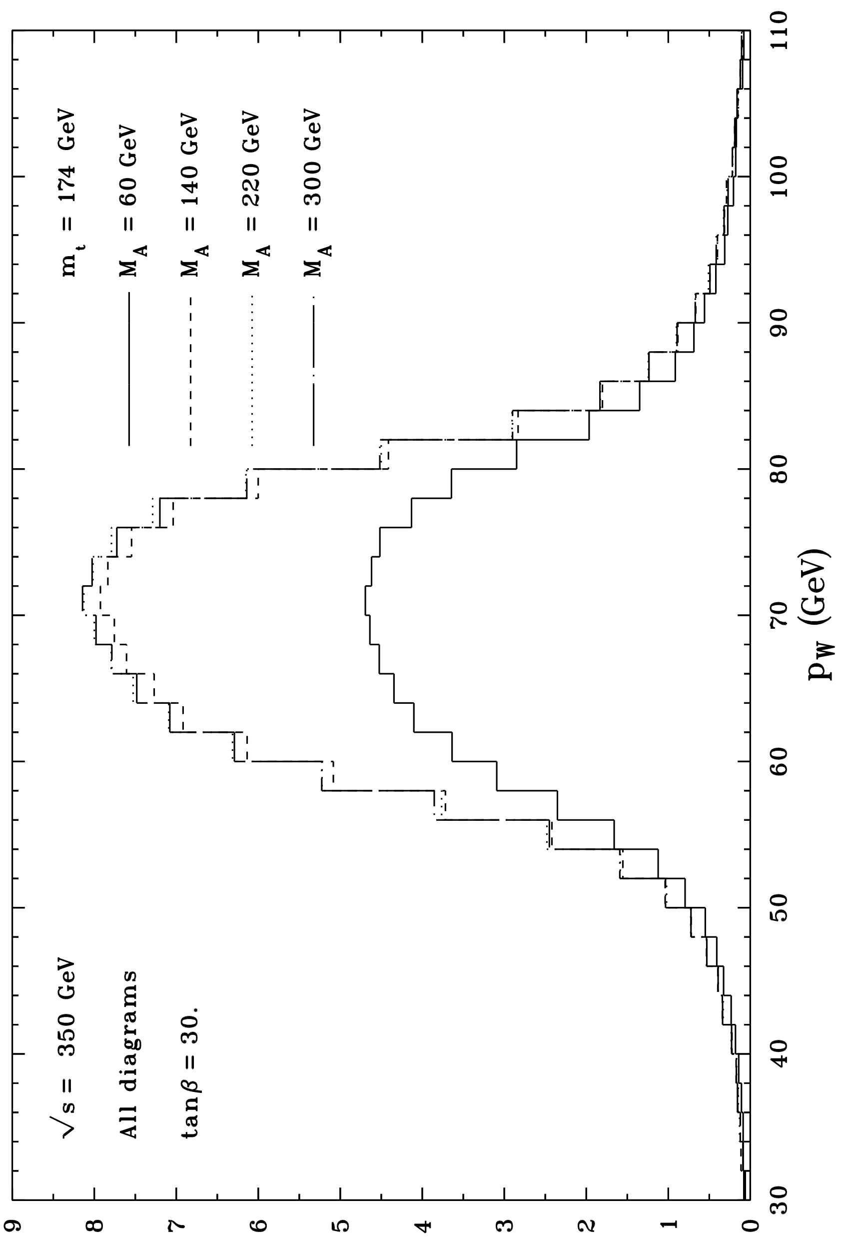

√s = 350 GeV
All diagrams
tanβ = 30.
m_t = 174 GeV
M_A = 60 GeV
M_A = 140 GeV
M_A = 220 GeV
M_A = 300 GeV
dσ/ dp_W (fb/GeV)
p_W (GeV)

Fig. 5a

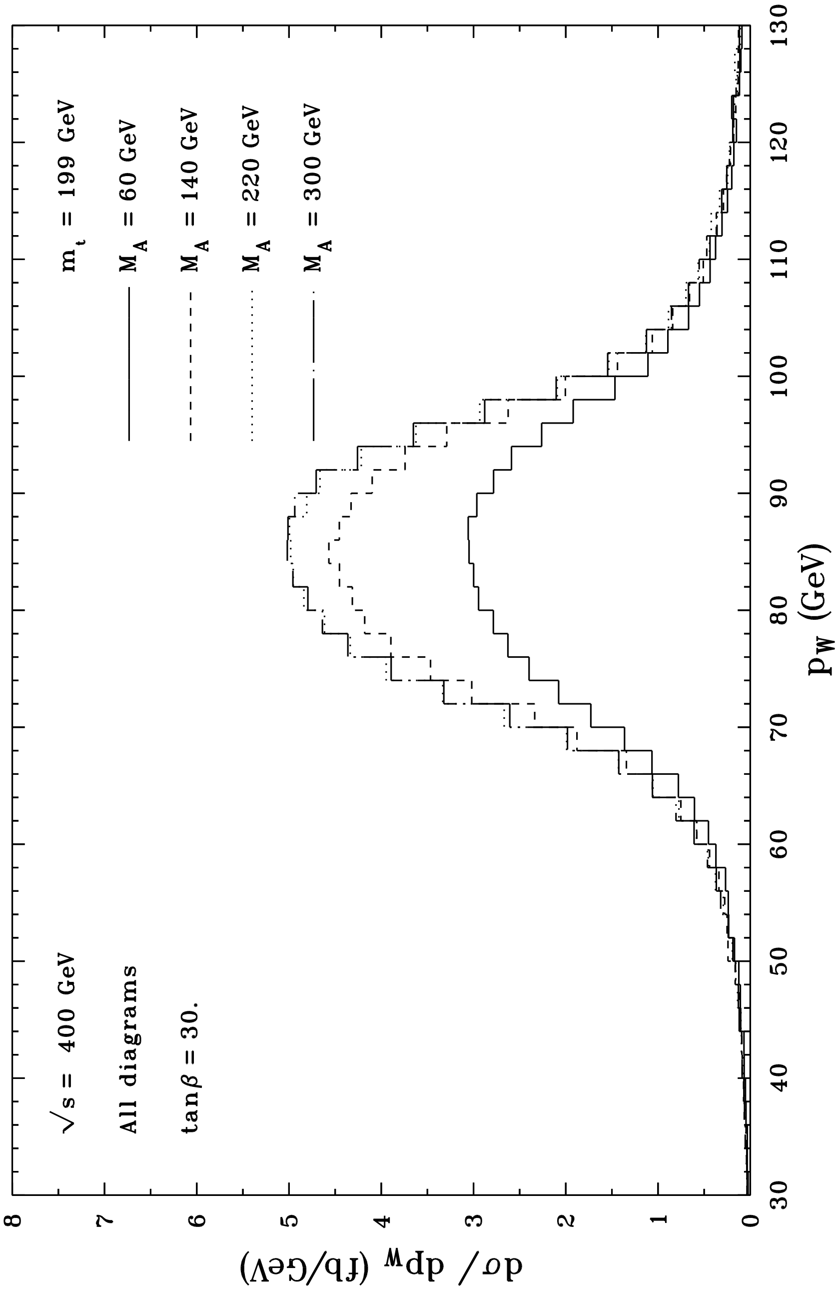

$\sqrt{s}$ = 400 GeV
All diagrams
tanβ = 30.
m_t = 199 GeV
M_A = 60 GeV
M_A = 140 GeV
M_A = 220 GeV
M_A = 300 GeV
$d\sigma/\ dp_W$ (fb/GeV)
p_W (GeV)
0
1
2
3
4
5
6
7
8
30
40
50
60
70
80
90
100
110
120
130

Fig. 5b

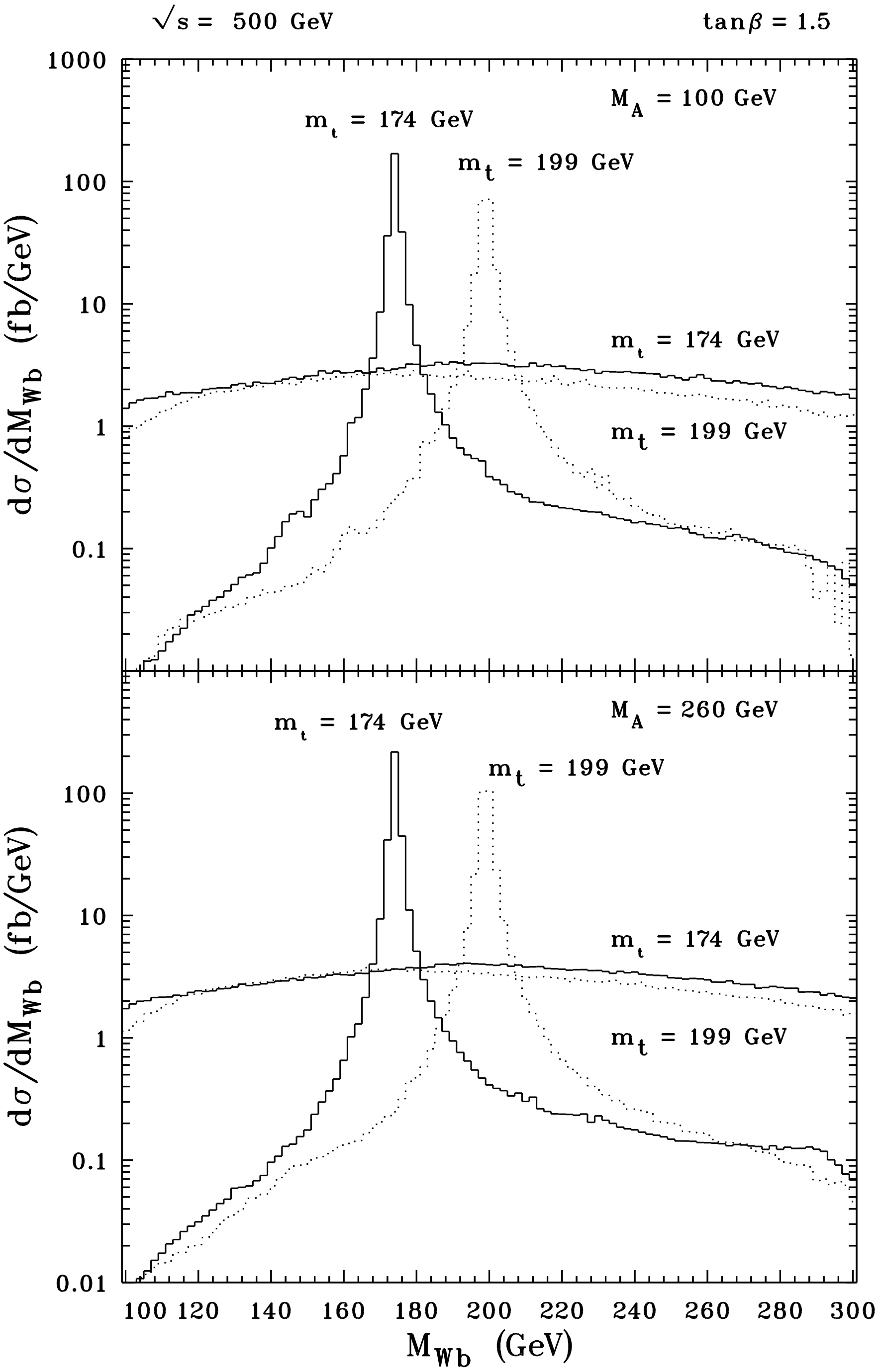

$\sqrt{s}$ = 500 GeV
tanβ = 1.5
M_A = 100 GeV
m_t = 174 GeV
m_t = 199 GeV
m_t = 174 GeV
m_t = 199 GeV
M_A = 260 GeV
m_t = 174 GeV
m_t = 199 GeV
m_t = 174 GeV
m_t = 199 GeV
$d\sigma/dM_{Wb}$ (fb/GeV)
M_{Wb} (GeV)

Fig. 6a

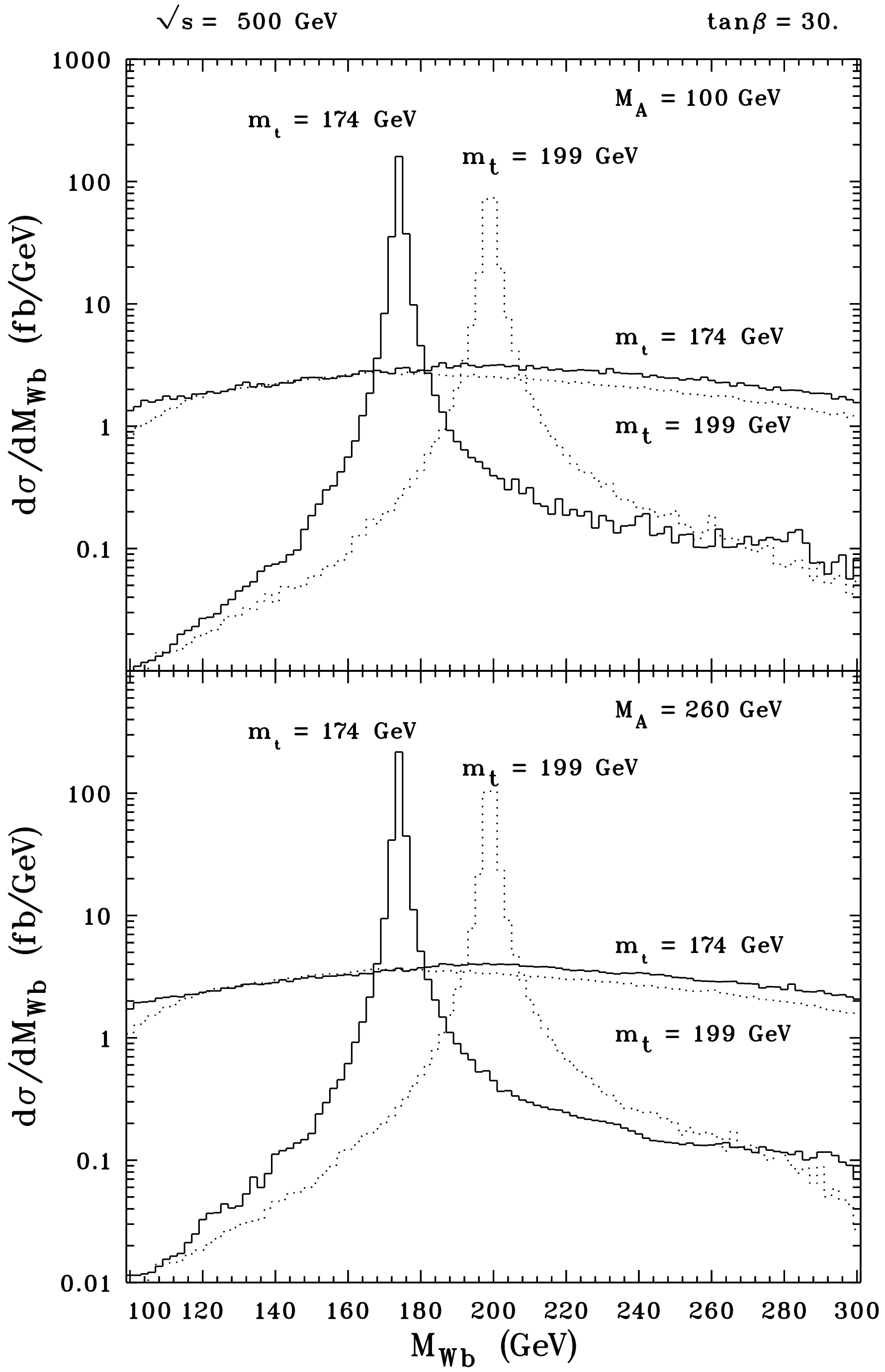

√s = 500 GeV
tanβ = 30.
M_A = 100 GeV
m_t = 174 GeV
m_t = 199 GeV
m_t = 174 GeV
m_t = 199 GeV
M_A = 260 GeV
m_t = 174 GeV
m_t = 199 GeV
m_t = 174 GeV
m_t = 199 GeV
dσ/dM_Wb (fb/GeV)
dσ/dM_Wb (fb/GeV)
1000
100
10
1
0.1
100
10
1
0.1
0.01
100 120 140 160 180 200 220 240 260 280 300
M_Wb (GeV)

Fig. 6b

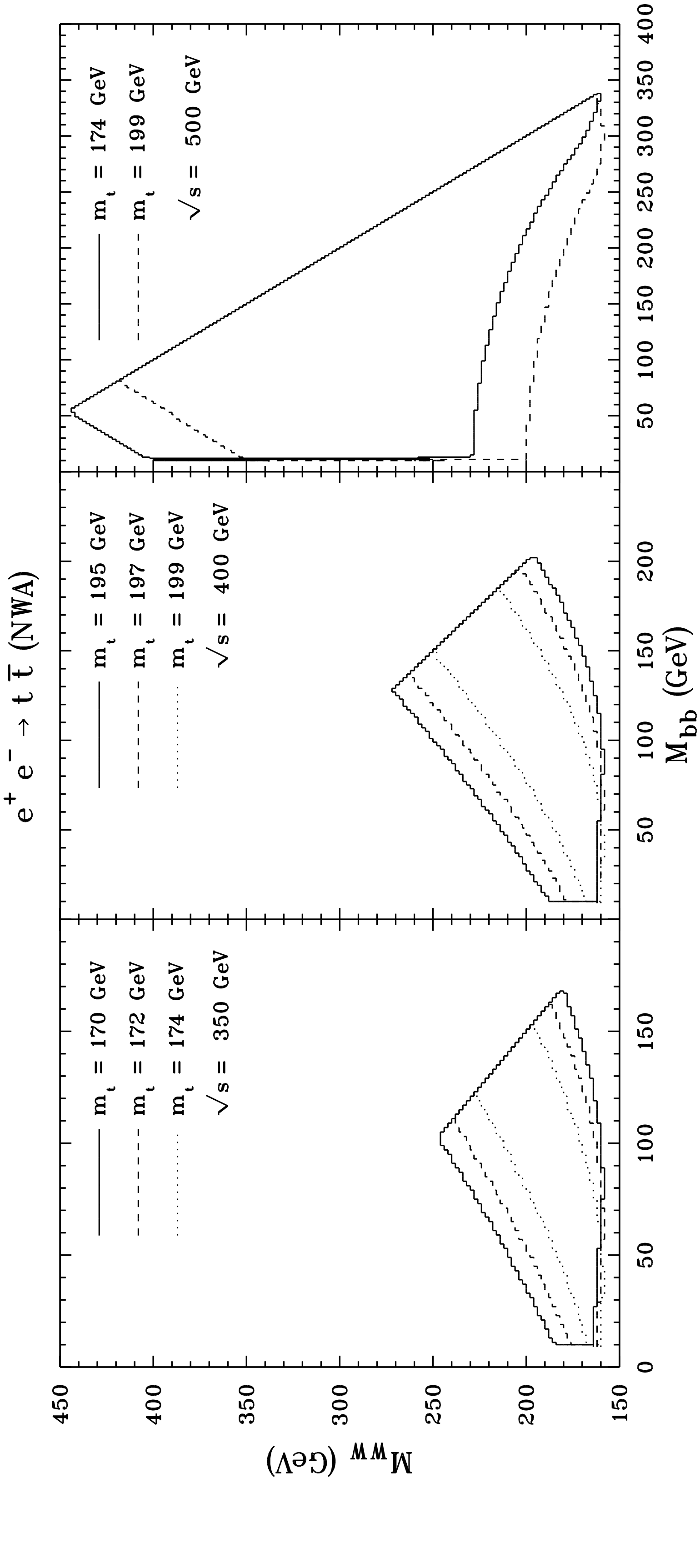

e⁺ e⁻ → t t̄ (NWA)
m_t = 170 GeV
m_t = 172 GeV
m_t = 174 GeV
√s = 350 GeV
m_t = 195 GeV
m_t = 197 GeV
m_t = 199 GeV
√s = 400 GeV
m_t = 174 GeV
m_t = 199 GeV
√s = 500 GeV
M_bb (GeV)
M_WW (GeV)

Fig. 7

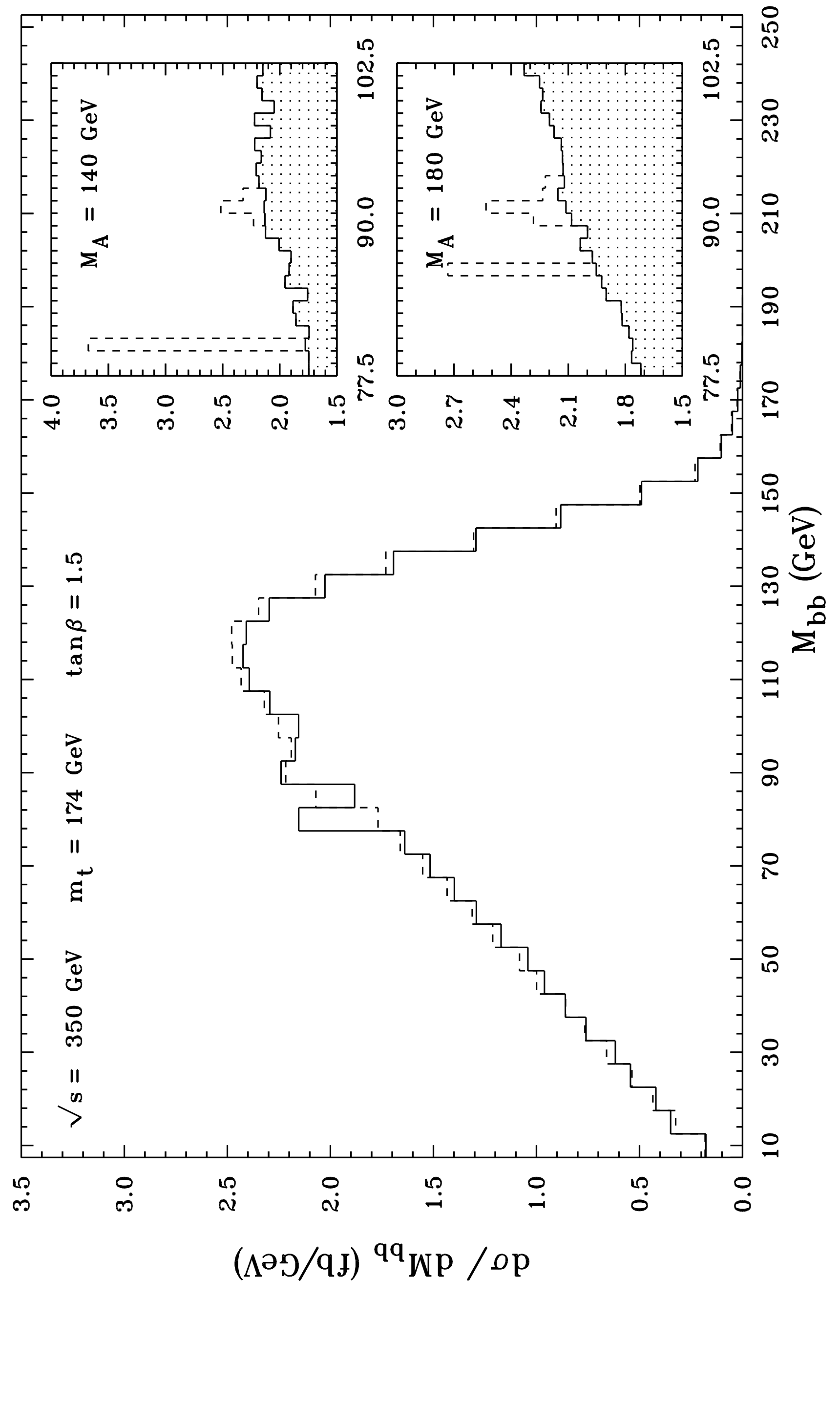

√s = 350 GeV
m_t = 174 GeV
tanβ = 1.5
M_A = 140 GeV
M_A = 180 GeV
M_bb (GeV)
dσ/ dM_bb (fb/GeV)

Fig. 8a

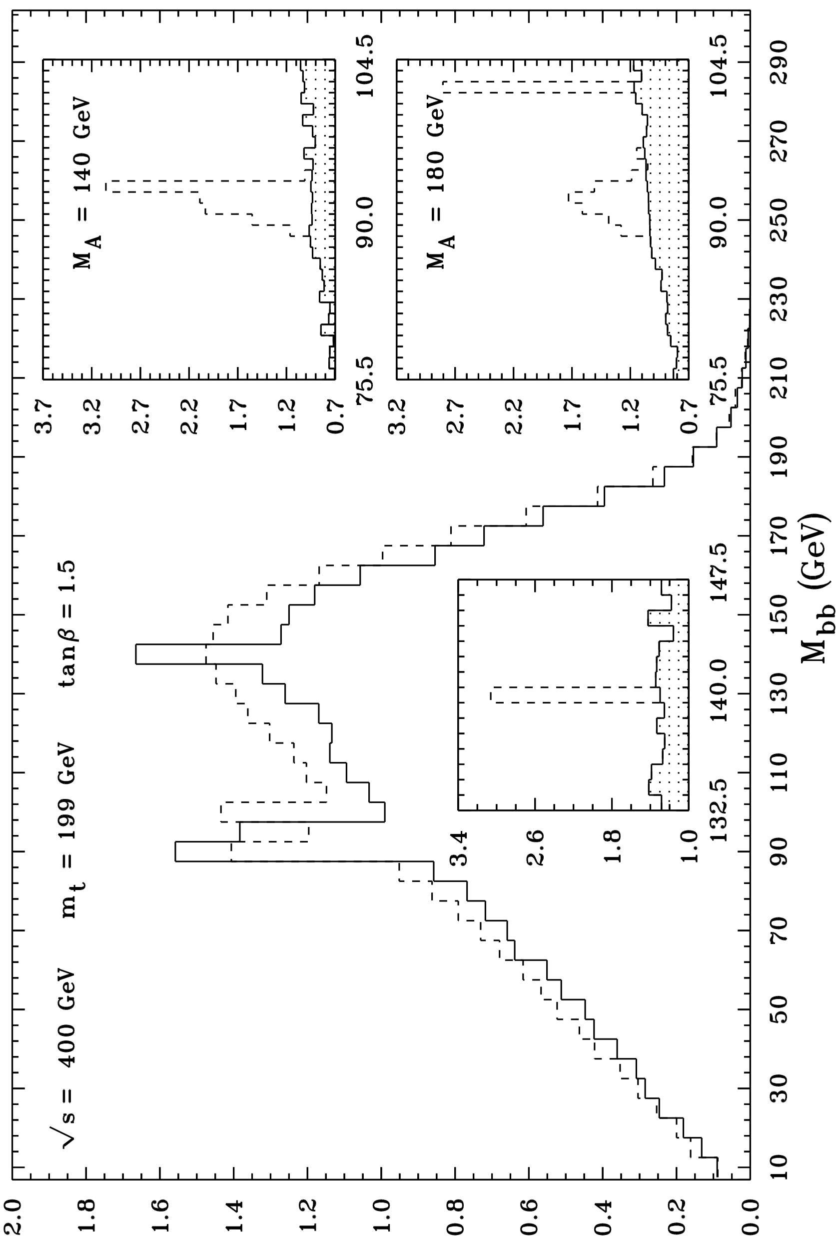

√s = 400 GeV
m_t = 199 GeV
tanβ = 1.5
M_A = 140 GeV
M_A = 180 GeV
dσ/ dM_bb (fb/GeV)
M_bb (GeV)

Fig. 8b

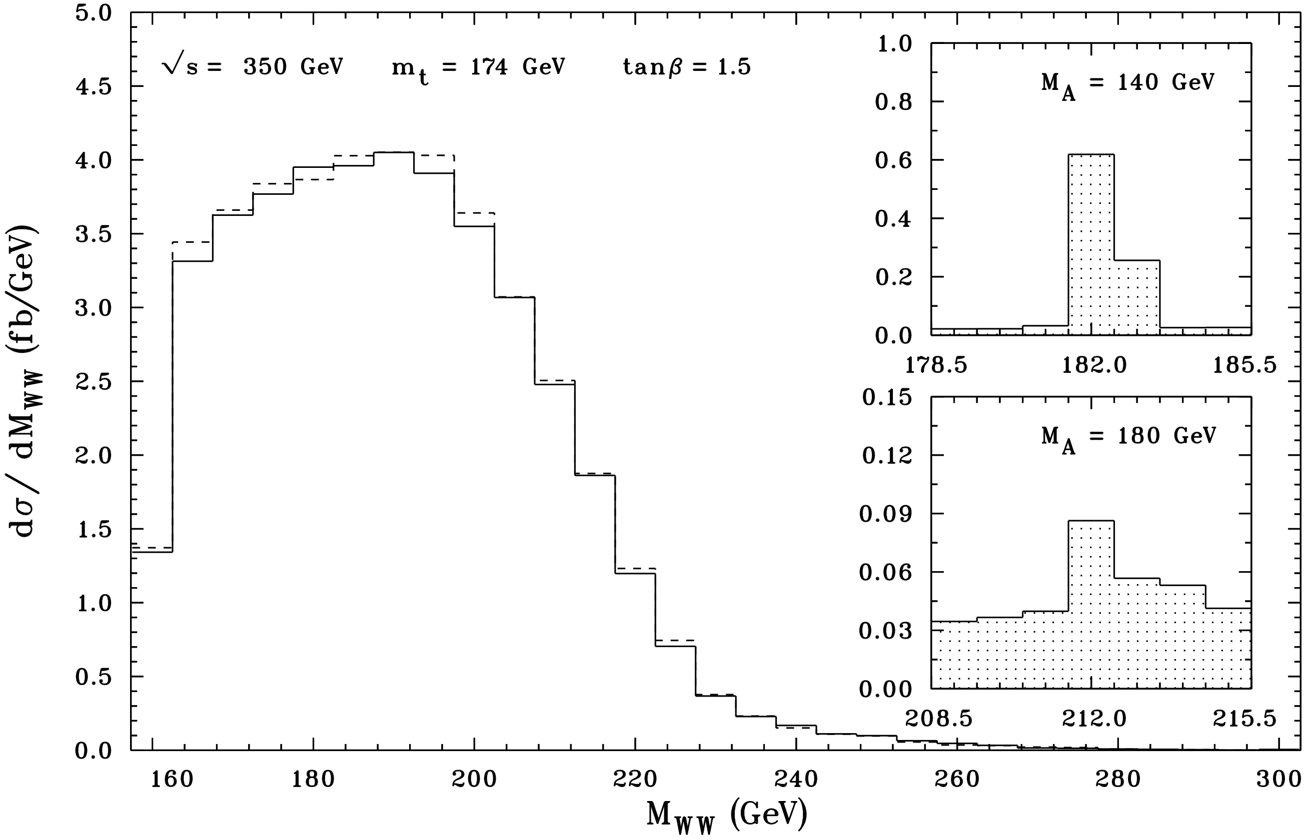

$\sqrt{s}$ = 350 GeV
m_t = 174 GeV
$\tan\beta$ = 1.5
$d\sigma / dM_{WW}$ (fb/GeV)
M_{WW} (GeV)
M_A = 140 GeV
M_A = 180 GeV

Fig. 9a

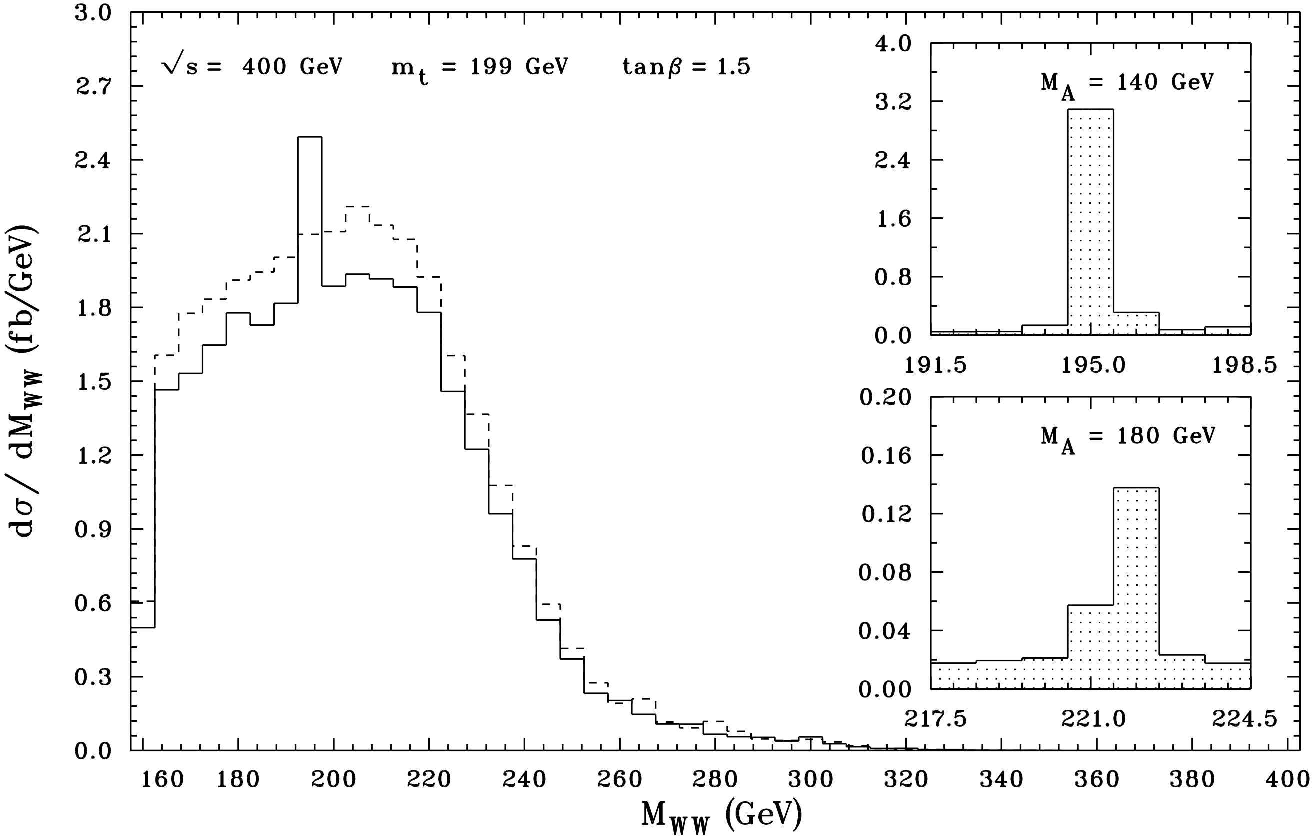

$\sqrt{s}$ = 400 GeV
m_t = 199 GeV
$\tan\beta$ = 1.5
M_A = 140 GeV
M_A = 180 GeV
$d\sigma/\,dM_{WW}$ (fb/GeV)
M_{WW} (GeV)

Fig. 9b

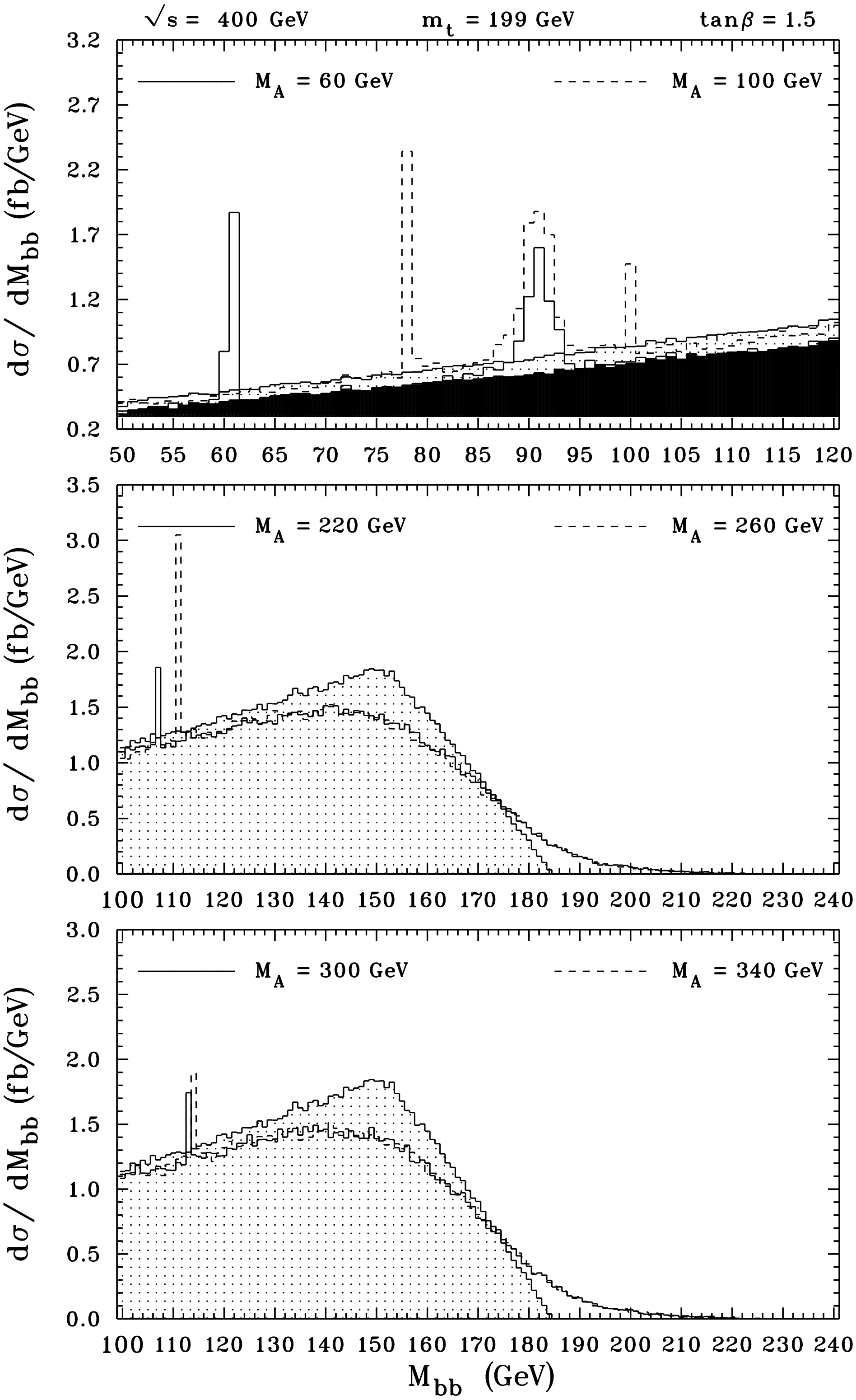

$\sqrt{s}$ = 400 GeV
m_t = 199 GeV
tanβ = 1.5
M_A = 60 GeV
M_A = 100 GeV
M_A = 220 GeV
M_A = 260 GeV
M_A = 300 GeV
M_A = 340 GeV
dσ/ dM_{bb} (fb/GeV)
M_{bb} (GeV)

Fig. 10

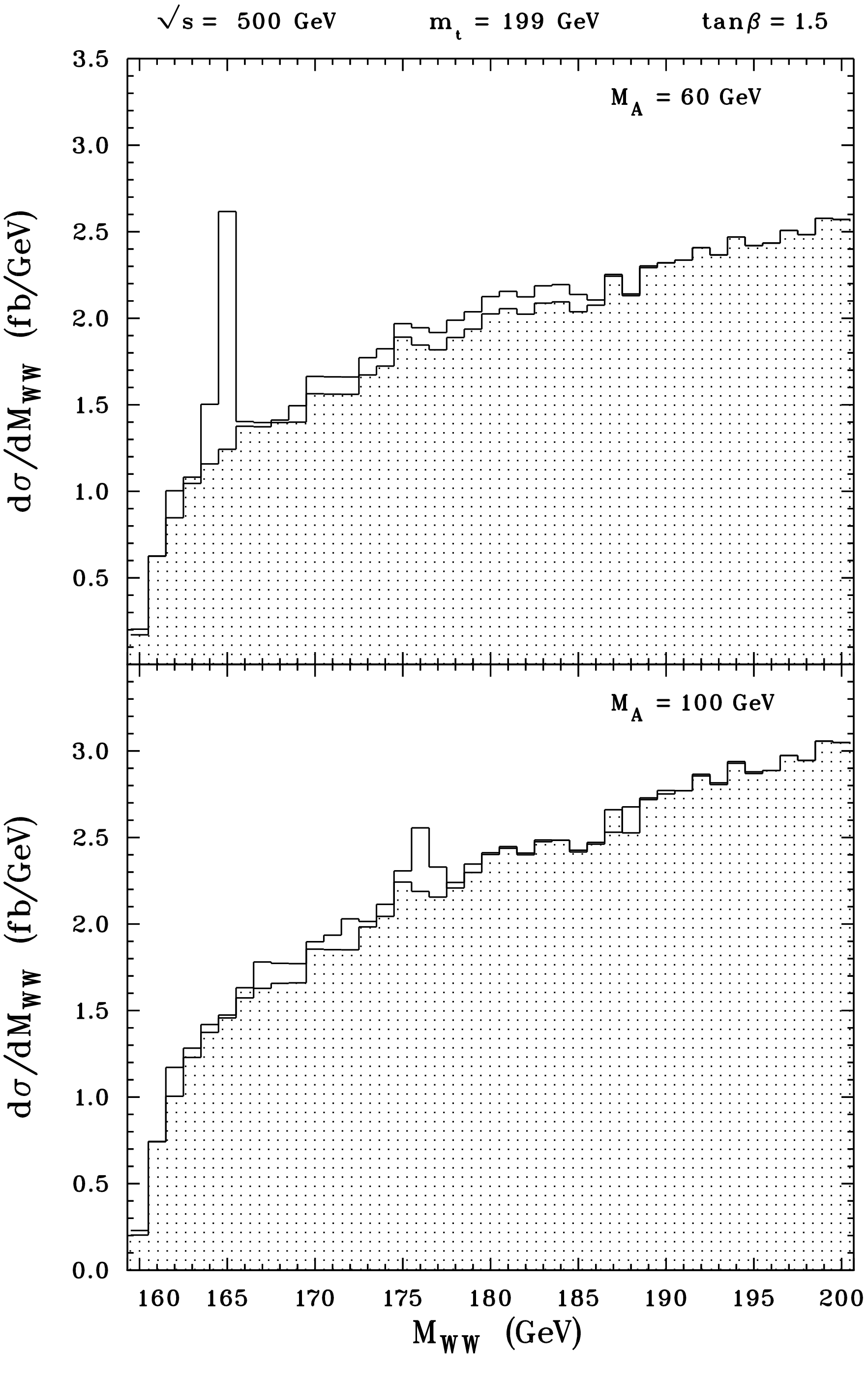

√s = 500 GeV
m_t = 199 GeV
tanβ = 1.5
M_A = 60 GeV
M_A = 100 GeV
dσ/dM_WW (fb/GeV)
dσ/dM_WW (fb/GeV)
M_WW (GeV)
3.5
3.0
2.5
2.0
1.5
1.0
0.5
0.0
160
165
170
175
180
185
190
195
200

Fig. 11